

Initiations of Mesoscale Convective Systems in the Middle Reaches of the Yangtze River Basin Based on FY-4A Satellite Data: Statistical Characteristics and Environmental Conditions

**Yanan Fu ^{1,2}, Jianhua Sun ^{1,2,3}, Shenming Fu ⁴, Yuanchun Zhang ¹,
Zheng Ma ¹**

¹ Key Laboratory of Cloud-Precipitation Physics and Severe Storms, Institute of Atmospheric Physics, Chinese Academy of Sciences, Beijing, China

² University of Chinese Academy of Sciences, Beijing, China

³ Collaborative Innovation Center on Forecast and Evaluation of Meteorological Disasters, Nanjing University of Information Science and Technology, Nanjing, Jiangsu Province, China

⁴ International Center for Climate and Environment Sciences, Institute of Atmospheric Physics, Chinese Academy of Sciences, Beijing, China

Corresponding author: Dr. Jianhua Sun (sjh@mail.iap.ac.cn)

Key Points

- The initiations of mesoscale convective systems are backward tracked through a hybrid method of areal overlapping and optical flow
- Quasistationary and outward-moving mesoscale convective systems show notable differences in initiation and developments
- A synoptic circulation pattern associated with the Mei-yu front is most favorable for the initiation of mesoscale convective systems

Abstract

Based on the brightness temperature observed by the Fengyun-4A satellite, eight hundred mesoscale convective systems (MCSs) are identified in the middle reaches of the Yangtze River Basin during the warm seasons (April–September) of 2018–2021, and these MCSs are categorized into the quasistationary (QS) type and the outward-moving (OM; i.e., moving beyond the source region) type. Afterwards, the initiations of the MCSs are backward tracked using a hybrid method of areal overlapping and optical flow. Then, the main features of QS-MCSs and OM-MCSs and their respective synoptic circulations and environmental parameters are analyzed. The QS-MCSs primarily occur in July and August and are mainly initiated in the afternoon. The OM-MCSs mostly occur in June and July with two initiation peaks appeared at noon and late night, respectively. The QS-MCSs are mainly initiated in mountainous areas. In contrast, the OM-MCSs are mainly initiated in plain areas. Compared to the OM-MCSs, the QS-MCSs show notable diurnal variation in intensity and develop more rapidly. Circulations of a total of 285 days (without direct influences from tropical cyclones) are objectively classified into three patterns by using the k-means algorithm. Pattern-I, which is closely related to low-level jets, shows the most similar features to those of typical Mei-yu fronts, and it acts as the most favorable circulation type for MCS initiations. Pattern-II is dominated by northwesterlies, with a relatively stable layer in the low-level troposphere. Pattern-III features a dry-adiabatic or even a superadiabatic layer that contributes to decreasing the layer stability.

Plain Language Summary

Mesoscale convective systems (MCSs) often cause severe convective weather over the middle reaches of the Yangtze River Basin and pose a great threat to life and property in this region. This study identified and tracked MCSs using satellite data and categorized them into the quasistationary (QS) type and the outward-moving (OM) type based on their movement features. The QS-MCSs primarily occurs in July and August and is mainly initiated in the afternoon over mountains. The OM-MCSs mostly occurs in June and July and is mainly initiated at noon and late night over the plains. Compared to the OM-MCSs, the QS-MCSs show notable diurnal variation in intensity and develop more rapidly. Large-scale circulation regulates environmental conditions and further affects the initiation of MCSs. Circulations over the middle reaches of the Yangtze

River Basin are classified into three patterns, each of which is dominated by a large-scale weather system. The circulation pattern dominated by the Mei-yu front is the most favorable for MCS initiation. The circulation pattern dominated by the northwesterly is favorable for the initiation of OM-MCSs but not for QS-MCSs. The circulation pattern dominated by the southerly produces a strong thermal effect and is favorable for the initiation of QS-MCSs.

1 Introduction

Severe convective weather phenomena, such as heavy rainfall, hailstorms, wind gusts and tornadoes, are mainly associated with mesoscale convective systems (MCSs) (Houze, 2004; Maddox, 1980; Zheng et al., 2013). The generalized concept of the MCS usually covers broad temporal and spatial scales (Yang et al., 2015), and MCSs exhibit different forms if different techniques of detection and identification are employed. In conventional weather maps, MCSs are generally presented as mesoscale high/low pressures (Zipser, 1977). Based on precipitation observations, MCSs often appear as mesoscale rain clusters or belts (Shen et al., 2020). However, MCSs usually appear as different radar reflectivity morphologies (Gallus et al., 2008; Ma et al., 2021a; Yang & Sun, 2018). On satellite infrared images, MCSs often appear as cold-cloud shields (CCSs) with a certain temporal and spatial scale (Laing & Fritsch, 1997; Machado et al., 1998; Meng et al., 2021; Yang et al., 2015; Zheng et al., 2008).

Using the criteria of brightness temperature and cloud area, Maddox (1980) detected a kind of meso- α scale convective system, which was later known as the mesoscale convective complex (MCC), and since then, the method based on the criteria of brightness temperature and cloud area has been widely used in research on MCCs (Laing & Fritsch, 1997; Miller & Fritsch, 1991; Rodgers et al., 1983; Velasco & Fritsch, 1987). Augustine and Howard (1988) simplified the method of Maddox (1980) and found that applying the criteria of brightness temperature ≤ -52 °C and cloud area $\geq 5 \times 10^4$ km² could better describe the evolution of storms. In recent years, -52 °C has been used as the brightness temperature criterion to identify MCSs (Kukulies et al., 2021; Morake et al., 2021; Yang et al., 2015; Yang R. et al., 2020; Meng et al., 2021), and different cloud area and duration criteria have been applied to determine the spatial and temporal scales of MCSs.

Williams and Houze (1987) developed an algorithm to track an individual cloud

cluster in two successive infrared images by calculating the overlapping rate of the two cloud areas, and since then, the areal overlapping method has been widely used in MCS tracking. Morel and Senesi (2002) improved the accuracy of MCS tracking by estimating the movement of clouds and developed the ISIS (satellite imagery tracking instrument) algorithm. Feng et al. (2018) improved the tracking accuracy by expanding the area of the target cloud and developed the FLEXTRKR (flexible object tracker) algorithm. In addition, the optical flow approach has been widely used since it was introduced into meteorology research, including the nowcasting of precipitation (Bowler et al., 2004; Bechini & Chandrasekar, 2017) and the improvement of numerical forecast results (Marzban & Sandgathe, 2010). In recent years, the optical flow approach has been applied in the research of new generation geostationary satellite products. Vandal and Nemani (2020) improved the temporal resolution of 10.8 μm infrared longwave radiation products of the new generation Geostationary Operational Environmental Satellite from 15 min to 1 min using the optical flow approach, and they successfully captured the evolution of a severe convective event. Burton et al. (2022) applied the optical flow approach to satellite-retrieved rainfall rate products for West Africa, and extrapolations showed useful skill at up to 4 h of lead time. In the present study, the areal overlapping method is used to track MCSs, and the optical flow is calculated to help improve accuracy.

Previous studies have mainly focused on the process from the formation to the termination of an MCS. Due to the data resolution and technical method limitations, few studies have focused on the initiation of an MCS. Roberts and Rutledge (2003) suggested that the precursor signal of convection initiation (CI) can be captured on satellites. Subsequently, two algorithms for identifying precursor signals and predicting CI based on satellite observations were developed, namely, the SATCAST (satellite convection analysis and tracking algorithm) algorithm (Mecikalski & Bedka, 2006) and the UWCI (University of Wisconsin Convective Initiation) algorithm (Sieglaff et al., 2011). Both scientific research and operational practice have shown that the initiation of MCSs can be identified through satellite observations.

As mentioned above, MCSs have a wide spectrum of spatial and temporal scales, and the features of MCSs, such as the cloud extent, cloud top temperature and cloud motion, vary worldwide (Feng et al., 2019; Kolios & Feidas, 2010; Morel & Senesi, 2002; Punkka & Bister, 2015; Rehbein et al., 2018). The activities of MCSs in China

have regional characteristics: the highest frequency of MCSs over the Tibetan Plateau occurs in July (Zhang et al., 2021; Jiang & Fan, 2002; Mai et al., 2020) and formed mainly in the afternoon (Zheng et al., 2008); the activities of MCSs in the North China Plain are the most frequent in June, July and August, and the formations occur mostly around noon (Ma et al., 2021a); under the influence of sea–land breeze, the MCSs in South China propagate offshore (inland) at night (in the daytime) (Bai et al., 2020; Zheng et al., 2008).

The initiation, development, and organization of MCSs are controlled and regulated by synoptic and mesoscale circulations. Lewis and Gray (2010) found that MCSs in Britain are mainly affected by three types of circulations and that the organization of MCSs is related to the interaction of perturbations at the upper level and warm advections at the lower level. Peters and Schumacher (2014) divided the circulations favorable for MCSs in the Great Plains of the United States into warm season-type and synoptic-type circulations. The synoptic-type MCSs tended to occur downstream of a progressive upper-level trough along a low-level potential temperature gradient with the warmest air to the south and southeast. Warm-season-type MCSs typically occurred within the right-entrance of a minimally to anticyclonically curved upper-level jet along a low-level potential temperature gradient with the warmest air to the southwest. Song et al. (2019) found that the favorable environments for MCSs over the Great Plains of the United States have frontal characteristics and enhanced low-level jets, while the unfavorable environments feature enhanced upper-level ridges. Sugimoto and Ueno (2010) found that MCSs over the eastern Tibetan Plateau mainly occurred under the condition of the eastward extension of the upper tropospheric anticyclone with the enhancement of near-surface low pressure in the western plateau. He et al. (2017) classified the circulation patterns over central East China into nine typical types based on the geopotential height fields at 850 hPa, and MCSs mainly occurred in the meridional circulations, which were associated with the Western North Pacific Subtropical High to the east and a low-pressure system to the west. Maurer et al. (2017) identified one particular MCS initiation in the Sahel that large-scale convergence forces smaller convective cells initiated at multiple locations merging into one larger MCS.

Diurnal variations in appearance frequency of the cloud clusters have been found over different regions of East Asia (Akiyama, 1989; Asai et al., 1998; Kato et al., 1995;

Li et al., 2007; Takeda & Iwasaki, 1987). Takeda & Iwasaki (1987) found that mesoscale cloud clusters (i.e., MCSs in our study) observed over the ocean tend to form frequently from midnight to early morning, whereas mesoscale cloud clusters over the continent tend to form from afternoon to evening, which might be associated with the difference between radiative processes over the continent and those over the ocean. Akiyama (1989) found that mesoscale cloud clusters tend to develop in the basin areas (in the high-altitude regions) in the morning (in the afternoon), suggesting that the condition of the underlying surface not only causes the different diurnal variations over the continent and the ocean, but also over basin areas and mountainous areas, as we also found in the current study.

The aforementioned studies show that different synoptic circulations often lead to different environmental conditions, and the interactions of environmental conditions, topography, underlying surface and other factors are highly nonlinear, which makes it difficult to forecast the initiation and development of MCSs. Previous studies involving the MCS life cycle are still limited in terms of understanding its formation. At present, thanks to high spatial-temporal resolution satellite data, the development of an MCS from initiation to formation can be accurately captured through backward tracking. The middle reaches of the Yangtze River Basin (YRB) are located in the transitional zone between the second-step terrain (mountains) and the plains over East China, with complicated orography and various underlying surfaces. The Mei-yu fronts are very active in this area, and their precipitation and convection have unique characteristics and complicated mechanisms (Fu et al., 2011b; Sun & Zhang, 2012; Wang et al., 2021; Zhang et al., 2014; Zhang et al., 2020). In the present study, the MCSs over the middle reaches of the YRB are identified and tracked first, and then, the MCS initiation is detected through backward tracking. Next, the temporal-spatial distribution and features of the MCSs are investigated. Finally, the synoptic circulations in this region are objectively classified into different patterns to find the circulations and environmental conditions favorable for the initiation of an MCS. The remainder of this paper is organized as follows. Section 2 introduces the data and methodologies. Section 3 presents the statistics of MCSs, including the temporal-spatial distributions of initiation and apparent features during their life cycles. Section 4 presents the objective classification of circulations in the middle reaches of the YRB and examines the circulation patterns and environmental conditions favorable for MCS initiation. Finally,

a summary is given in Section 5.

2 Data and methodology

2.1 Data and focus area

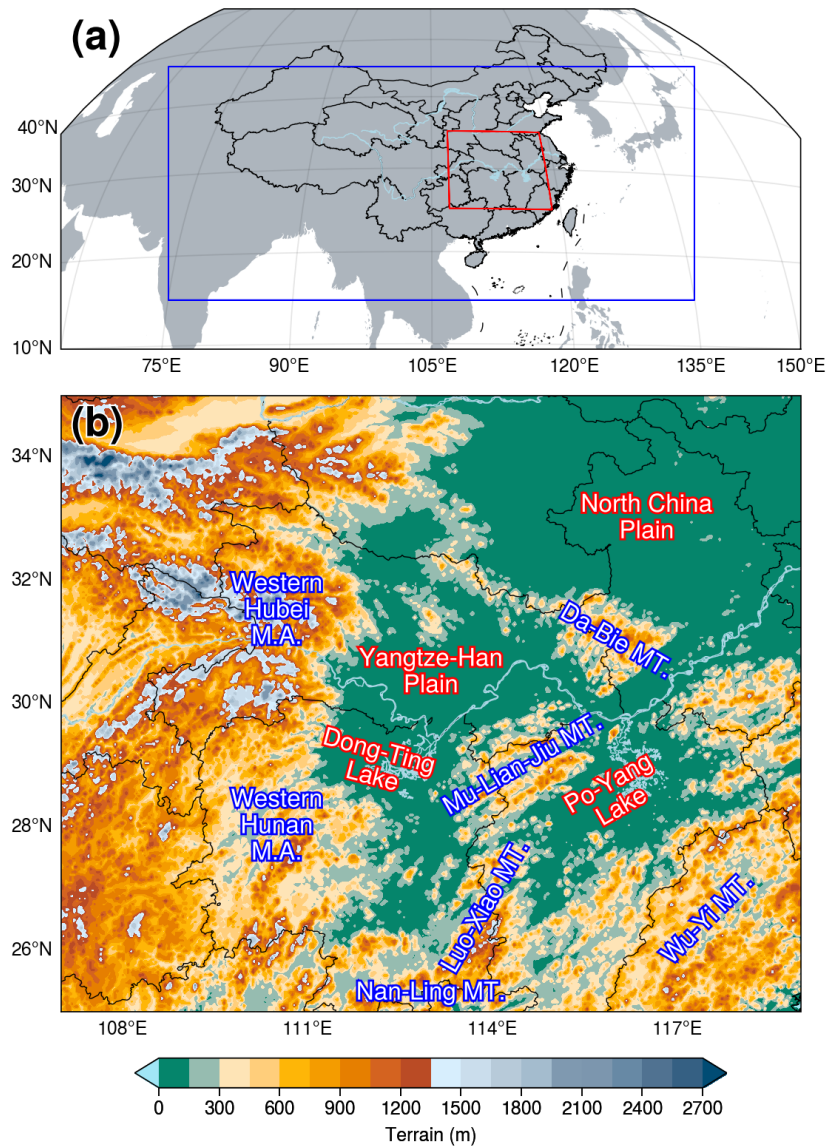
The brightness temperature (BT) at the 10.8 μm band of the Advanced Geosynchronous Radiation Imager onboard the Fengyun-4A (FY-4A) satellite is used to identify and track MCSs in the present study. The spatial resolution of FY-4A BT data is 4 km at nadir. The temporal resolution of regional observations over China and its surrounding area is ~ 5 min (Yang et al., 2017). The BT fields used in the present study are limited to the region (~ 15 – 45°N and 75 – 135°E) shown in Fig. 1a to ensure consistency in the dataset. The integrities of the dataset during the warm season (April–September) of 2018–2021 are 93.26%, 97.65%, 97.07%, and 98.05%, respectively, with an average integrity of 94.51%.

Considering that the mechanisms of the convection related to tropical cyclones (TCs) are different from those of extratropical convection (Bister, 2001; Hendricks & Montgomery, 2006; Rodgers et al., 1991), MCSs induced by TCs and circulations related to TCs are excluded using the TC best-track dataset provided by the China Meteorological Administration, and the temporal resolution is 3 h (Lu et al., 2021; Ying et al., 2014).

The fifth-generation ECMWF (European Centre for Medium Range Forecasts) reanalysis (ERA5) data, with a temporal resolution of 1 h and a spatial resolution of 0.25° (Hersbach et al., 2020), are used in the classification and composite analysis of circulations. The construction of proximity soundings is mainly based on ERA5 data. However, considering the differences in the boundary layer variables between reanalysis and observed soundings (Gensini et al., 2014; King & Kennedy, 2019), correcting the boundary layer variables of the reanalysis sounding is necessary. Therefore, the present study uses the 1-h observations of automatic weather stations (AWSs) provided by the China Meteorological Administration to correct the surface level of the ERA5 data before constructing proximity soundings.

The middle reaches of the YRB are defined as the region covering 107 – 119°E and 25 – 35°N in the present study (Fig. 1a), and the orography (Fig. 1b) in this area is complicated. The western Hubei mountainous areas and western Hunan mountainous

216 areas are located in the west, the Nan-Ling Mountains are in the south and the Wu-Yi
 217 Mountains are in the southeast. The North China Plain is in the northeastern part of this
 218 region. Three smaller plains are in the middle, namely, the Jiang-Han Plain, the Dong-
 219 Ting Lake Plain and the Po-Yang Lake Plain, with the Da-Bie Mountains, the Mu-Lian-
 220 Jiu Mountains and the Luo-Xiao Mountains distributed from north to south.



221

222 **Figure 1.** (a) The coverage of BT data (blue rectangle) in the present study and the
 223 boundary of the middle reaches of the YRB (red line). (b) The terrain height (m) in the
 224 middle reaches of the YRB. Mountains (MT.) and mountain areas (M.A.) are labeled in
 225 blue, and plains and lakes are labeled in red.

226

2.2 Identification and tracking methods

227 Following Yang R. et al. (2020), the criteria and steps used in the present study
228 to identify MCS are outlined as follows (Fig. 2): 1) detect CCSs with temperature \leq
229 -52°C and extent $\geq 5000 \text{ km}^2$ in the BT fields; 2) track CCSs at different time steps;
230 and 3) continuous CCSs that last longer than 3 h are identified as MCSs. The first (last)
231 time that an MCS satisfies the above criteria is considered to be MCS formation
232 (termination). The time when the CCS of an MCS reaches its maximum extent is
233 considered to be MCS maturity.

234 The combination of areal overlap and optical flow is used in the present study
235 to track CCSs with the following steps: 1) calculate the optical flow between two
236 successive BT fields; 2) extrapolate the target CCS at the previous time by adding
237 optical flow and compare it with the CCSs at the later time, and the one with an
238 overlapping rate $\geq 30\%$ is considered the successor of the target CCS; 3) if two CCSs
239 or more satisfy the criterion of the areal overlapping rate at the later time, the one with
240 the highest overlapping rate will be considered the successor of the target CCS; 4)
241 examine the TC locations derived from the best-track dataset, and if there are any TC-
242 related clouds within the coverage of a CCS, the CCS will be excluded because the
243 CCS is a TC cloud instead of an MCS. Backward tracking is applied to find the
244 initiation time and location of an MCS. Considering that the CCS is small and develops
245 rapidly during the early stage of an MCS, no areal limitation has been applied during
246 backward tracking.

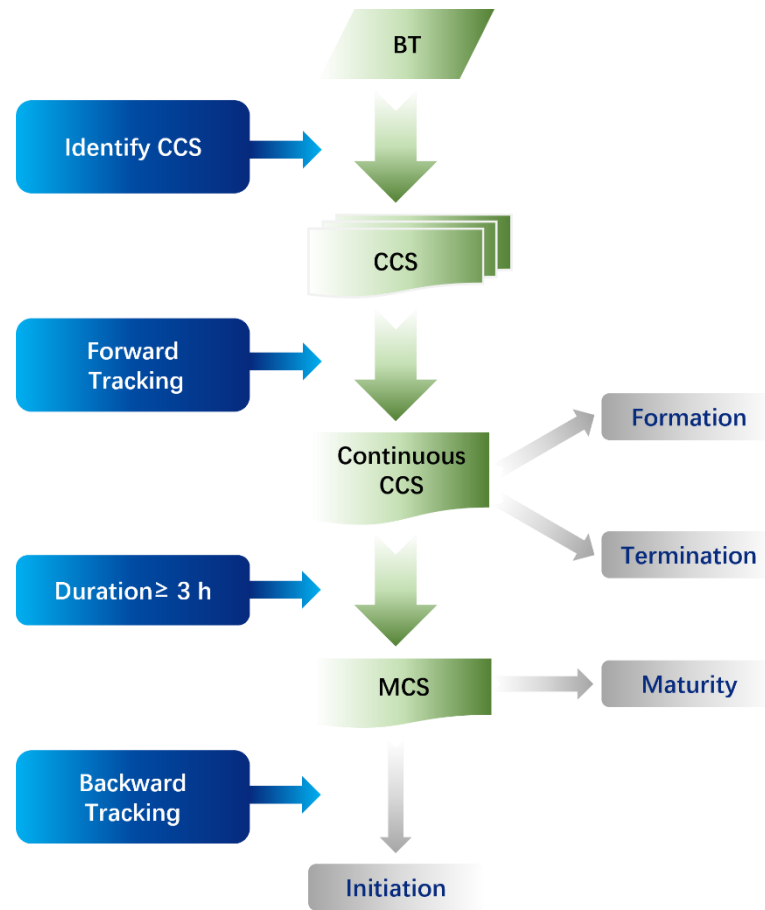


Figure 2. Flow chart of MCS identification and tracking.

2.3 Filtering of backward tracking

Backward tracking may not be accurate because the extent of a CCS is small and the motion is fast during the early stage of an MCS. The splitting and regeneration of MCSs, cirrus anvils, and deficiency of BT data may all lead to incorrect backward tracking. Therefore, further examinations are conducted on the backward tracking results. If two or more MCSs are initiated at the same time and location, it is considered that those MCSs are split from the same MCS or that one MCS is regenerated from another. Then, the initiation will be assigned to the earliest MCS according to the formation time, and the remaining MCSs will be regarded as inaccurate tracking and excluded from the MCS dataset. For the inaccurate backward tracking results caused by deficiency of BT data, the filtering approach is outlined as follows: check whether the BT data before the initiation time are missing; if true, the result will be regarded as inaccurate and excluded from the MCS dataset. CCSs connected with cirrus anvils are manually checked since they vary greatly between two successive times.

2.4 Objective classification

The *k-means* algorithm, which is widely used for classification in atmospheric research due to its stable performance (Hoffmann & Schlünzen, 2013; Huth et al., 2008; Kanungo et al., 2002; Ku et al., 2021; Solman & Menéndez, 2003; Stahl et al., 2006; Zhang et al., 1997), is applied in the present study for the objective classification of circulation patterns. The meteorological variable used for classification in the present study is the geopotential height field at 700 hPa. The geopotential height field is a commonly used variable in circulation classification (Hoffmann & Schlünzen, 2013; Liu et al., 2019; Miao et al., 2017; Ning et al., 2020; Yang et al., 2021). Huth et al. (2008) suggested that due to a high degree of dependence among individual levels, the inclusion of additional levels yields little extra information over using a single level, which has been confirmed in many studies (Dong et al., 2020; Liu et al., 2019; Miao et al., 2017; Ning et al., 2020; Yang et al., 2021). The isobaric layer of 700 hPa is chosen mainly considering that the isobaric layer of 850 hPa and below may be influenced by the topography, of which the average altitude is ~1200 m over the mountainous areas in the middle reaches of the YRB. Statistics (see Section 3) in the present study suggest that MCSs are mainly initiated between 0300–0600 (Coordinated Universal Time, UTC) and that 78.4% (627 out of 800) of MCSs occur in June, July and August (JJA). In addition, circulation patterns vary greatly in September (Tao 1980). Therefore, the geopotential height fields at 700 hPa at 0000 UTC each day during JJA of 2018–2021 are used for circulation classification. TCs may have a great impact on synoptic circulations, leading to inaccurate classification results. Therefore, based on the TC locations derived from best-track data, if a TC enters the area west of 124 °E and north of 20 °N on a certain day, this day will be recorded as a TC-day and will be excluded during circulation classification. A total of 83 TC days are excluded.

The silhouette coefficient (Rousseeuw, 1987) is calculated as an approach to evaluate the performance of different classification numbers. The silhouette coefficient considers both the homogeneity within a class and the difference between classes (Huth

et al., 2008; Rousseeuw, 1987) and is widely used as criterion to determine the classification number (Bernard et al., 2013; Nga et al., 2021; Ternynck et al., 2016). The optimal choice of classification number in the present study is 3 based on the evaluation of the silhouette coefficient.

2.5 Construction of proximity soundings

Considering the coarse temporal-spatial resolutions of the observed radiosonde data, the environmental parameters in the present study are calculated from the reanalysis-derived proximity soundings based on ERA5 data. However, some previous studies have noted the differences in the boundary layer variables between reanalysis and observed soundings and that correcting the boundary layer variables of the reanalysis sounding is necessary (Gensini et al., 2014; King & Kennedy, 2019). Therefore, the hourly AWS observations are used to correct surface-level variables in ERA5 data before calculating environmental parameters.

The nearest hour before an MCS initiation and the ERA5 grid closest to the initiation are chosen as the time and location, respectively, to construct a proximity sounding. The closest AWS observation to the ERA5 grid within a radius of 100 km of the grid is selected to correct the surface-level variables of the ERA5 data. The ERA5 temperature/dew-point temperature profile is first constructed based on the isobaric layers (all 37 layers from 1000 hPa to 1 hPa). Then, the isobaric layers below the AWS surface pressure layer are neglected, and the AWS variables are deemed the lowest layer of the proximity sounding (Brooks et al., 2003; Ma et al., 2021b; Yang & Sun, 2018).

The environmental parameters are calculated based on proximity soundings to investigate the dynamic and thermodynamic conditions of MCS initiation under different circulation backgrounds. Ten parameters are selected, namely, the surface-based convective available potential energy (SBCAPE), the most unstable layer convective available potential energy (MUCAPE), surface-based convective inhibition (SBCIN), most unstable layer convective inhibition (SBCIN), lifted index (LI), lifted condensation level (LCL), level of free convection (LFC), precipitable water (PW), 0–3 km bulk wind shear (SHR3) and 0–6 km bulk wind shear (SHR6). These parameters, with clear physical meanings and good performances in distinguishing between different intensities and types of convection, are widely used in convection environment

studies (Brotzge et al., 2013; Grams et al., 2012; J. C. Kirkpatrick et al., 2007; Ma et al., 2021b; McCaul & Weisman, 2001; Yang & Sun, 2018).

3 Statistical characteristics

3.1 MCS trajectories and paths

On the one hand, the movements and propagations of MCSs are closely related to the occurrences of convective weather phenomena; on the other hand, they represent the regulation of large-scale circulations over mesoscale systems (Li et al., 2008; Yang J. et al., 2020; Jiang & Fan, 2002; Mai et al., 2020). In the present study, MCSs are categorized into quasistationary (QS) and outward-moving (OM) types. For QS MCSs, both the formations and terminations occur within the study area (Fig. 1b), and OM MCSs refer to those formed within the study area but terminated outside of the study area.

During the warm seasons (April–September) of 2018–2021, 800 MCSs are identified in the middle reaches of the YRB, where 524 are QS type and 276 are OM type, accounting for 65.5% and 34.5% of the total MCSs, respectively. Based on the movement trajectories of the MCSs, those of the QS type (Fig. 3a) are short and mainly within the study area. Part (13.7%) of the QS MCSs moved outside of the study area at certain times during their life cycles; however, they moved back into and terminated within the study area. The trajectories of OM MCSs (Fig. 3b) are longer than those of QS MCSs and are mainly eastward and southward. Most of the OM MCSs terminated after propagating into the oceanic area; however, some OM MCSs with long trajectories could reach the Pacific Ocean east of Japan or north of the Indo-China Peninsula.

To further investigate the main paths of the two types of MCSs, the *k-means* algorithm is adopted to classify MCS trajectories. Based on the evaluation of the silhouette coefficient, the trajectories of QS (OM) MCSs are classified into four (three) kinds of main paths. Among the four kinds of paths of the QS MCSs (Fig. 3c), the number of MCSs in the southeast kind is the largest, and the northwest kind is the smallest. The lengths of the northeast and southeast kinds are long, while those of the northwest and southwest kinds are short. Except for the northwest kind with the smallest number of MCSs, the other three kinds of paths all move from the mountains to the plains. The phenomenon that convective cells are initiated in mountainous areas

and propagate to the plains often occurs in the Rocky Mountains and the Great Plains of the United States (Carbone et al., 2002; Zhang et al., 2014) and the Tai-Hang Mountains and the North China Plain (He & Zhang, 2010; Zhu et al., 2018), which is related to the mountain-plain solenoid driven by thermodynamic effects (Bao et al., 2011; Sun & Zhang, 2012; Zhang & Sun, 2017). For the OM MCSs, among the three kinds of paths (Fig. 3d), the number of MCSs in the southeast kind is the largest. The northeast kind has the longest length, followed by the southeast kind, and the southwest kind has the shortest length.

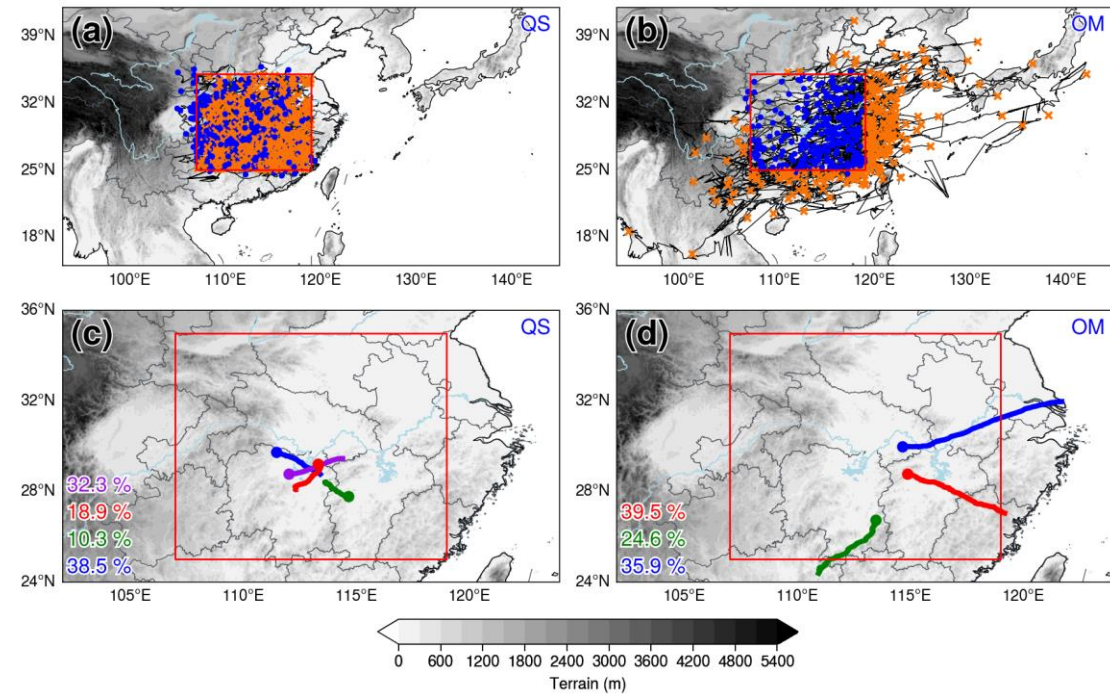


Figure 3. The movement trajectories of QS MCSs (a) and OM MCSs (b) and the composite movement paths of QS MCSs (c) and OM MCSs (d). The blue dots (orange crosses) in (a) and (b) represent the initiation (termination) locations of MCSs. Different kind of paths are distinguished by different colors in (c) and (d), and the proportions of trajectories in different kinds are marked in the lower left corner. The gray shading represents terrain height (m). The red rectangle indicates the boundary of the middle reaches of the YRB.

3.2 Temporal-spatial distribution of MCS initiations

The temporal distributions of MCS initiation are shown in Fig. 4. The QS MCSs mostly occur in July, followed by August (Fig. 4a), while the OM MCSs occur most

frequently in July, followed by June (Fig. 4b). During the Mei-yu season in the YRB, namely, mid-June to mid-July (Tao, 1980), the mesoscale systems basically move eastward along the Mei-yu front. After mid-July, the convective cells in this area are mainly caused by local diabatic effects. These results explain why QS MCSs mostly occur in July and August, while OM MCSs mostly occur in June and July (Zhang et al., 2014). The QS MCSs are mainly (41.2%) initiated around noon (0400–0800 UTC), and the peak time is 0600–0700 UTC, which is identical in each month (Fig. 4a). However, the peak hours of initiation for OM MCSs vary in different months. In June and July, the initiation of OM MCSs has two peaks, one at noon (0300–0500 UTC) and the other at night (1800–1900 UTC). The noon peak is generally considered to be related to the instability caused by surface solar heating (Yu et al., 2007), and MCSs initiated during this time period correspond to the afternoon peak of summer precipitation in the YRB (Luo et al., 2016; Zhang et al., 2020). The mechanism for the late-night peak is complicated, which may result from instability due to nocturnal radiative cooling at the cloud top (Lin et al., 2000), water vapor accumulation at low levels in the evening (Kubota & Nitta, 2001), or diurnal variation in local circulation forced by complex terrain (He & Zhang, 2010; Li et al., 2005; Sun & Zhang, 2012; Zhang & Sun, 2017). Regardless of the triggering mechanism, the late-night initiation peak of the OM MCS corresponds to the morning peak of precipitation in the typical Mei-yu seasons (Luo et al., 2016; Zhang et al., 2020). In other months (except for September, which has only 4 MCSs), OM MCSs have only one peak in the afternoon (0600–0700 UTC), which is consistent with the QS type.

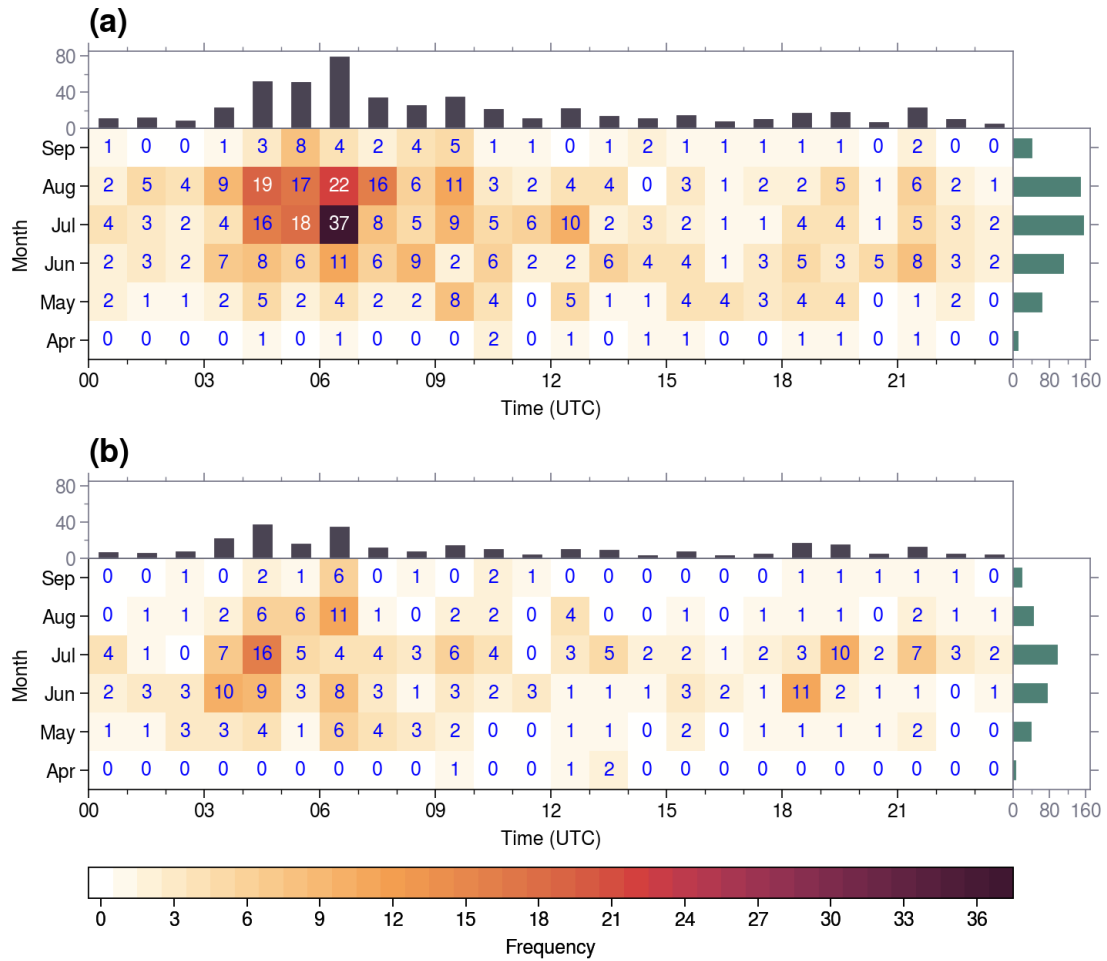


Figure 4. Monthly and diurnal distributions of the QS MCS frequency (a) and the OM MCS frequency (b) in the middle reaches of the YRB during the warm seasons (April–September) of 2018–2021. The horizontal axis represents the initiation time (UTC). The color shading symbolizes the occurrence frequency of MCSs.

The spatial distributions of MCS initiation are shown in Fig. 5. Both the QS MCSs (Fig. 5a) and the OM MCSs (Fig. 5b) are initiated mainly in the southern part of the YRB, which is consistent with a previous study (Zheng et al., 2008). Dividing the southern part of the YRB from the north roughly by 30 °N, 343 QS MCSs and 195 OM MCSs are initiated in the southern part of the YRB, accounting for 65.5% and 70.7% of their total amounts, respectively. The highest initiation frequency of QS MCSs is found over the western Hunan Mountains, the Mu-Lian-Jiu Mountains and the Luo-Xiao Mountains, while that of the OM MCSs is over the Po-Yang Lake Plain. The convection in mountainous areas is mainly driven by the thermodynamic forcing (Astling, 1984; Panosetti et al., 2016; Zhu et al., 2018), while in plain areas, due to the

lack of dynamic forcing or diabatic heating resulting from the complex terrain, the initiation of convection is mostly related to synoptic circulation systems (Reif & Bluestein, 2017; Wilson & Roberts, 2006), which explains why QS MCSs are more likely to be initiated over mountainous areas, while OM MCSs tend to be initiated over plain areas.

To better illustrate the spatial distributions of MCS initiation, July and August (June and July) are chosen as the high occurrence period for QS (OM) MCSs. For QS MCSs, the spatial distribution of initiation in July and August (Fig. 5c) is basically the same as in the entire warm season (Fig. 5a), and the highest initiation frequency is also over the western Hunan mountains, the Mu-Lian-Jiu Mountains and the Luo-Xiao Mountains (Fig. 1b), with the highest probability density of 0.015 (0.014 for the entire warm season). Although in-depth studies are required, this consistency further indicates that the initiation of QS MCSs in the middle reaches of the YRB may be caused by local topographic forced thermal circulation and thus varies little in different months. For the OM MCSs, the spatial distribution of initiation in June and July (Fig. 5d) exhibits some differences compared with that of the entire warm season (Fig. 5b). Over the Po-Yang Lake Plain (Fig. 1b), the maximum probability density increases from 0.017 to 0.022, indicating that in June and July, OM MCSs are more likely to be initiated over the plain areas. In addition, the probability density contours extend from the maximum over Po-Yang Lake to the southwest along the Luo-Xiao Mountains and to the southeast along the Wu-Yi Mountains (Fig. 1b) in the entire warm season, but in June and July, the probability density contours show fewer extensions outward from the maximum center, indicating that the initiation of OM MCSs is less related to the terrain in June and July.

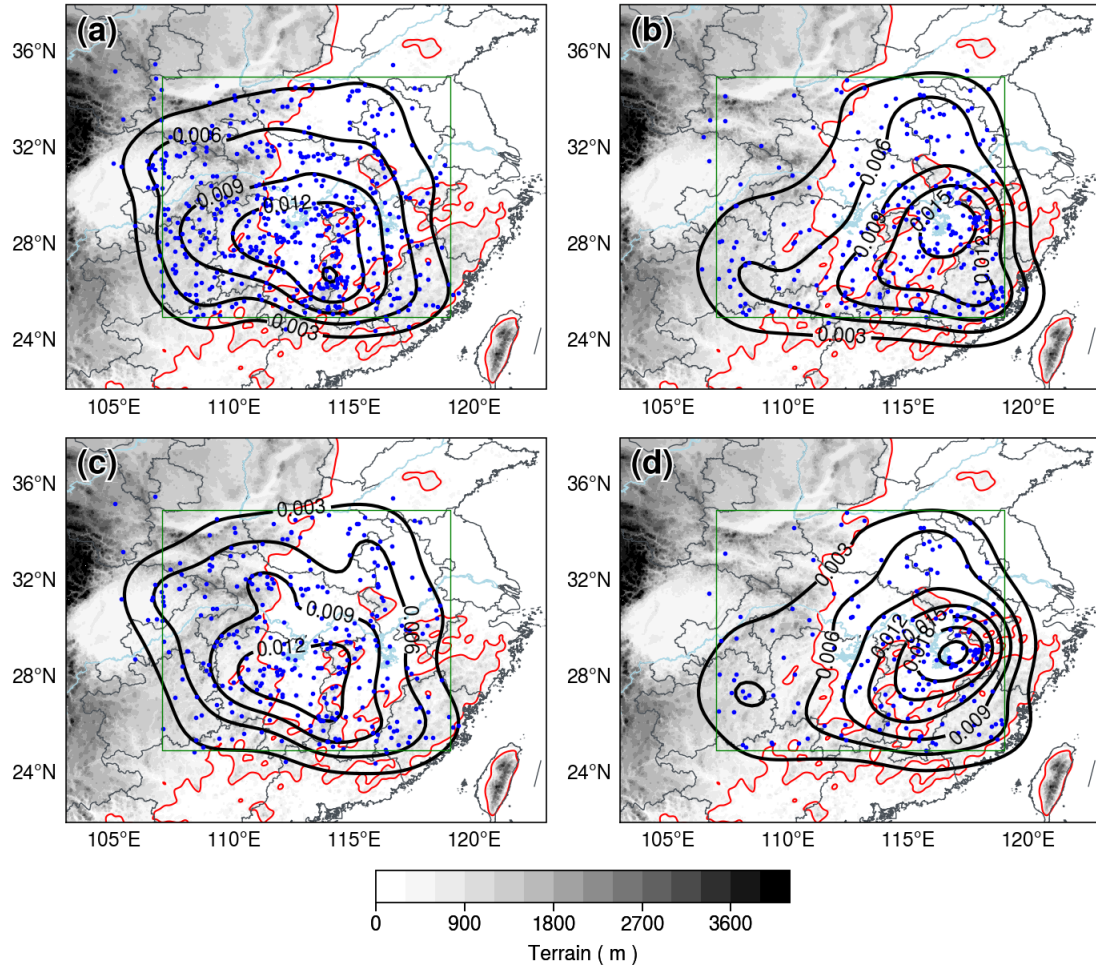


Figure 5. The spatial distribution of initiation locations of QS MCSs during the entire warm season (a) and in July and August (c) and OM MCSs during the entire warm season (b) and in June and July (d). The blue dots represent initiation locations, from which the spatial probability density is calculated and exhibited by the black contours. The green rectangle marks the middle reaches of the YRB. The gray shading represents terrain height (m) and the red contours denote the terrain height of 300 m.

3.3 Features of MCS movement

The moving velocity of an MCS between two consecutive times is calculated based on the centroid locations and the time interval. The average moving velocity of all times in the entire life cycle of an MCS is considered to be the bulk moving velocity of the MCS. In general, the speeds of OM MCSs are faster than those of QS MCSs (Fig. 6a). The movement of the MCS is regulated by the steering wind in the mid-lower troposphere (Rehbein et al., 2018); therefore, both the QS and OM MCSs move faster in April and May and slower in June, July and August. The speeds of the QS (OM)

MCSs are basically the same in July and August (June and July), indicating that the selection of a high occurrence period is reasonable. The speeds and directions of QS MCSs and OM MCSs in their high occurrence period are shown in Figs. 6 b and c. More than 80% of QS MCSs move at speeds of 0–45 km h⁻¹, and the highest proportion is located in the range of 15–30 km h⁻¹, accounting for 44% of all QS MCSs. Most (more than 70%) OM MCSs move at speeds of 15–60 km h⁻¹, with the highest proportion in the range of 30–45 km h⁻¹, accounting for 32%. The moving directions of the QS MCSs are relatively evenly distributed in all 8 directions in July and August with roughly similar proportions, which also indicates that the QS MCSs in July and August are less related to the activities of synoptic systems. The synoptic systems in the middle reaches of the YRB generally move eastward (Fu et al., 2011a; Zhang et al., 2018; Zhang & Sun, 2017), resulting in more than 50% of OM MCSs moving eastward and no OM MCS moving north or northwestward.

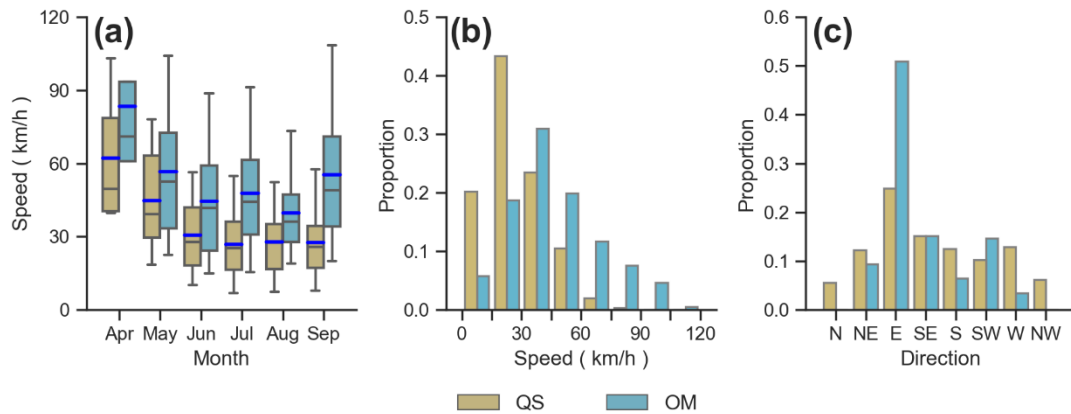


Figure 6. Box-and-whisker plot of MCS speed (a, km h⁻¹) during the warm seasons of 2018–2021 (a). The upper and lower edges (caps) of the boxes (whiskers) in the box-and-whisker plot represent the 3rd and 1st quartiles (95th and 5th percentiles), respectively. The black (blue) dashes inside boxes represent the medians (mean values). Histograms of MCS movement speeds (b, km h⁻¹) and directions (c) in the high occurrence period.

3.4 Duration, maximum extent and lowest temperature of MCSs

The duration and maximum extent represent the temporal-spatial scale of an MCS, and the lowest brightness temperature may reflect the intensity of the strongest convection in the MCS. In this section, box-and-whisker plots are applied to examine

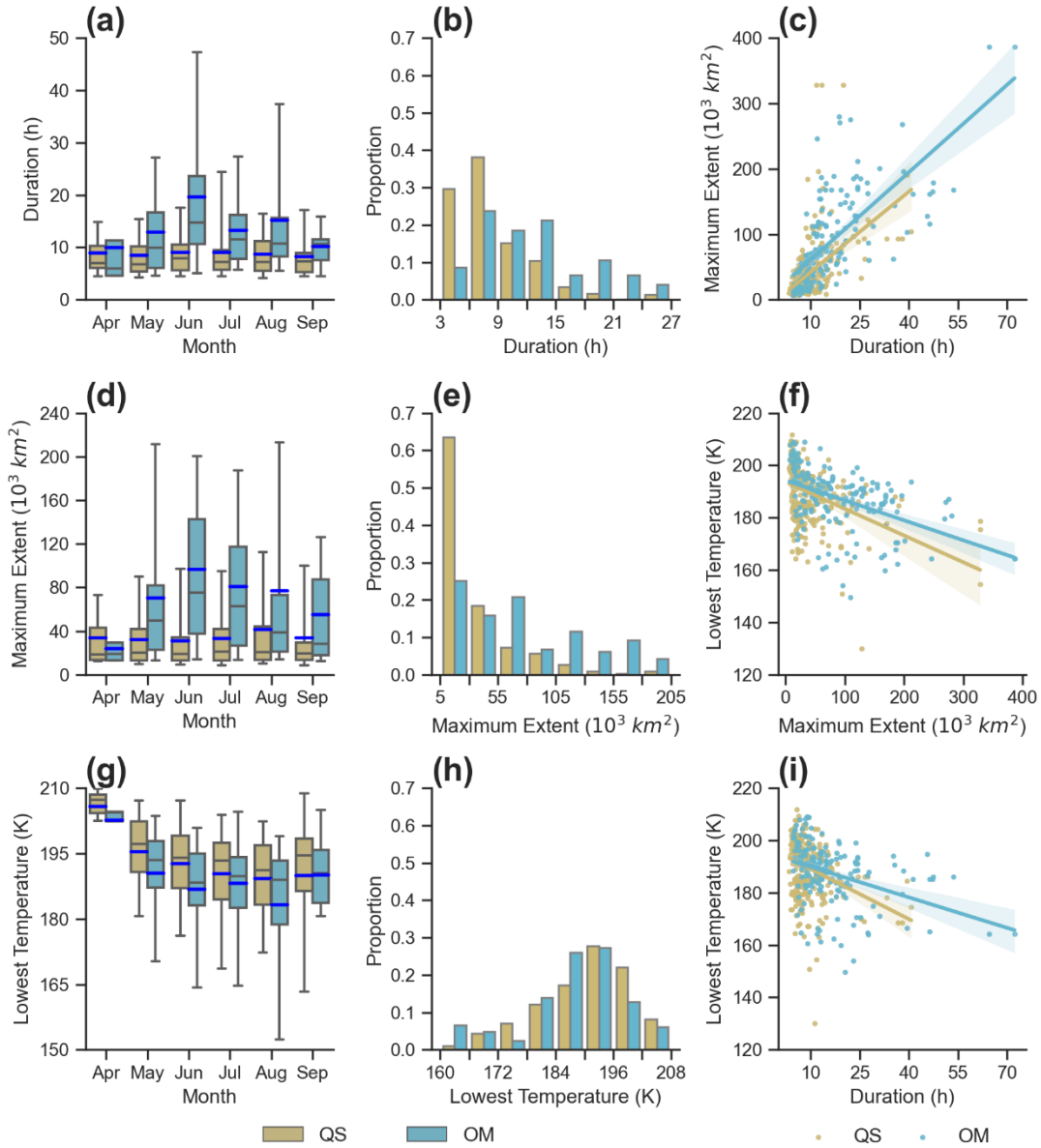
the distributions of the three features in the entire warm season (Figs. 7 a, d and g). Then, the proportion distributions (Figs. 7 b, e and h) and the pairwise relationships (Figs. 7 c, f and i) of these features in the high occurrence period (July and August for the QS MCSs and June and July for the OM MCSs) are analyzed.

Basically, the OM MCSs last longer than the QS MCSs (Fig. 7 a). The QS MCSs mainly last for 5–10 h, with no significant variations between different months. The OM MCSs in June last longer than those in other months, with an average duration of ~20 h. The maximum extents of QS MCSs are mainly smaller than $5 \times 10^4 \text{ km}^2$, while those of OM MCSs are mostly between $2 \times 10^4 \text{ km}^2$ and $1.5 \times 10^5 \text{ km}^2$ and vary from month to month. The lowest temperature shows a similar distribution between the QS MCSs and the OM MCSs with an average value of approximately 190 K. The mechanisms of initiation and development of QS MCSs may be related to the local topographically forced thermal circulation, resulting in little difference in duration and maximum extent between months. However, OM MCSs are mainly caused by synoptic systems that vary in different months in the middle reaches of the YRB (Wang et al., 2021; Sun et al., 2018), leading to complexity in the mechanisms of the initiation and development of OM MCSs, further resulting in differences in duration and maximum extent between months.

In July and August, nearly 40% of QS MCSs last 6–9 h and 30% last 3–6 h. In June and July, more than 60% of OM MCSs last 6–15 h, with ~20% of each 3-h interval. The maximum extents of QS MCSs in July and August are mainly 5×10^3 – $3 \times 10^4 \text{ km}^2$, accounting for more than 60%, while the maximum extents of the OM MCSs in June and July are distributed evenly in the 5×10^3 – $3 \times 10^4 \text{ km}^2$, 3×10^4 – $5.5 \times 10^4 \text{ km}^2$ and 5.5×10^4 – $8 \times 10^4 \text{ km}^2$ intervals, with each accounting for ~20%. For the lowest temperature, half of the QS (OM) MCSs are 184–196 K (190–202 K) in July and August (June and July).

Based on the above analysis, there are certain connections among the duration, maximum extent and lowest temperature of MCSs. The pairwise correlations of the three features in the high occurrence period are shown in Figs. 7 c, f and i. In general, the longer the durations of the MCSs are, the larger the maximum extents and the colder the cloud tops. With the extension of duration, the maximum extent shows an enlarging trend (Fig. 7c), which is consistent between the QS type and the OM type. With the

505 increase in the maximum extent, the lowest temperature decreases (Fig. 7f), and that of
 506 the QS type decreases faster than that of the OM type. With increasing duration, the
 507 lowest temperature shows a decreasing trend (Fig. 7i), and that of the QS MCSs also
 508 decreases faster.



509

510 **Figure 7.** The box-and-whisker plots on the left are the duration (a), the maximum
 511 extent (d) and the lowest temperature (g) of MCSs during the entire warm seasons of
 512 2018–2021. The upper and lower edges (caps) of the boxes (whiskers) in the box-and-
 513 whisker plot represent the 3rd and 1st quartiles (95th and 5th percentiles), respectively.
 514 The black (blue) dashes inside boxes represent the medians (mean values). The

histograms of the central column are the proportion of the duration (b), the maximum extent (e) and the lowest temperature (h) of MCSs in high occurrence periods of 2018–2021. The scatter plots on the right are the pairwise relationships between the duration and the maximum extent (c), the maximum extent and the lowest temperature (f), and the duration and the lowest temperature (i) in high occurrence periods of 2018–2021.

3.5 Diurnal variation in maximum extent and lowest temperature

Li et al. (2007) found that occurrence frequency and the intensity of the cloud clusters has diurnal variations. Therefore, to what extent do the QS MCSs and the OM MCSs differ from each other with regard to the diurnal variations in intensity? This question is addressed in this subsection.

To investigate the diurnal variation in the MCSs in the middle reaches of the YRB, the time when the maximum extent (lowest temperature) appears and the time span between MCS initiation and the maximum extent (lowest temperature) appearance are further examined. Since 58% of QS MCSs are initiated in July and August and 62% of OM MCSs occur in June and July, to highlight the difference between QS MCSs and OM MCSs, only MCSs in high occurrence periods are analyzed, and the results are shown in Fig. 8.

In July and August, the initiation frequency of QS MCSs peaks in the afternoon (0600–0700 UTC, Fig. 8a, upper subplot), which is the same as the result from the entire warm season (Fig. 3a). In June and July, the initiation frequency of OM MCSs has two peaks, namely, noon peak (0300–0500 UTC) and late-night peak (1800–2000 UTC, Fig. 8b, upper subplot). For the OM MCSs, compared with the result from the entire warm season (Fig. 3b), the proportions of MCS initiation during the noon peak (0300–0500 UTC) and the late-night peak (1800–2000 UTC) increase, but that during the afternoon peak (0600–0700 UTC) decreases.

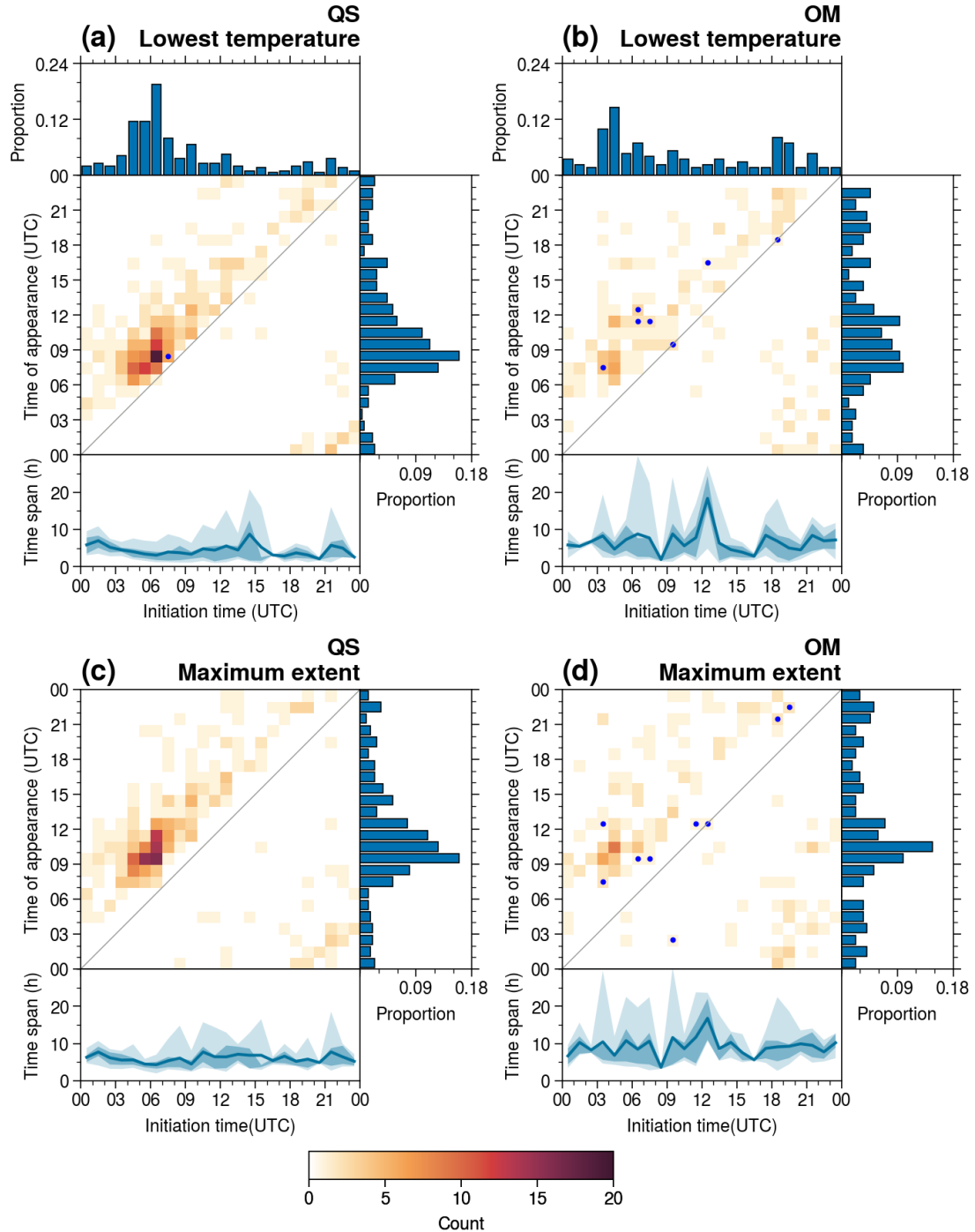
In July and August, the lowest temperatures of QS MCSs mainly appear in the afternoon (0700–1100 UTC), with a peak at 0800–0900 UTC (Fig. 8a, the main plot and the subplot on the right-hand side). The surface solar heating is the strongest in the afternoon; therefore, convective activities are most vigorous during this time period. In June and July, the lowest temperatures of OM MCSs mainly appear in the afternoon and the evening, distributed evenly during this time period without any obvious peak

(Fig. 8b, the main plot and the subplot on the right-hand side). As mentioned before, the mechanisms for convection development in the OM MCSs are complicated, resulting in no obvious peak for the lowest temperature appearance. In July and August, the maximum extents of QS MCSs mainly appear in the evening (0900–1200 UTC, Fig. 8c, the main plot and the subplot on the right-hand side), 1–2 h later than the appearance of the lowest temperature. In June and July, the maximum extents of OM MCSs mainly appear in the evening (0900–1100 UTC) (Fig. 8d, the main plot and the subplot on the right-hand side).

In July and August, the lowest temperatures (the maximum extents) of the QS MCSs appear 4.43 h (6.03 h) after initiation. The QS MCSs initiated at noon or in the afternoon (0500–1000 UTC) reach the lowest temperature ~3 h after initiation (Fig. 8a, lower subplot), which indicates that the QS MCSs initiated in this time period develop at roughly the same pace. The QS MCSs in July and August mainly achieve the maximum extent 4–7 h after initiation (Fig. 8c, lower subplot). In June and July, the lowest temperatures (maximum extents) of the OM MCSs appear 6.8 h (9.21 h) after initiation (lower subplots in Figs. 8 b and d). The development of OM MCSs is associated with many factors (i.e., synoptic systems, orography, and underlying surface) and interactions between these factors; therefore, the diurnal variations follow no obvious pattern.

Although Kato et al. (1995) have already pointed out that Cb-clusters around Central China show a remarkable diurnal variation in midsummer (i.e., late July to mid-August), differently from those during the Mei-yu season (i.e., mid-June to mid-July) which occur both during the daytime and at night, the analyses of Kato et al. (1995) are limited to the case study for 1979 with 6-h infrared images. In the present study, the QS-MCSs (OM-MCSs) occurring mainly in July and August (June and July), can be considered as the Cb-clusters appearing in midsummer (the Mei-yu season). The present study suggests that QS-MCSs and OM-MCSs show notable differences not only in diurnal variation, but also in characteristics, initiation and developments. In Kato et al. (1995), Cb-clusters occur both in the daytime and at night during the Mei-yu season. However, by using the data with much higher temporal resolution, the present study has drawn a more detailed and profound conclusion, that is, the initiation of OM-MCSs has two peaks, one at noon (0300–0500 UTC) and the other at night (1800–1900 UTC). The following part of this study will show that the above-mentioned diurnal variation

579 is related to the circulation patterns, the local diabatic effects and the topography. These
 580 new findings add much more detailed features and explanations to the results of Kato
 581 et al. (1995).



582

583 **Figure 8.** The two-dimensional histogram for the diurnal variation in the lowest
 584 temperature appearance of QS MCSs (a) and OM MCSs (b) and the maximum extent
 585 appearance of QS MCSs (c) and OM MCSs (d) in the high occurrence period of 2018–

2021. The main body of each plot exhibits the frequency of MCS initiation and the lowest temperature (maximum extent) in every hourly interval. The upper histogram exhibits the proportion of MCS initiation. The left histogram exhibits the proportion of the lowest temperature (maximum extent) appearance. The lower plot exhibits the time span between the lowest temperature (maximum extent) appearance and MCS initiation, with the solid line representing the mean time span and the light (dark) shading representing the 5%–95% (25%–75%) percentile interval. The blue dot indicates that the time span is longer than 24 h.

4 Circulation patterns and environmental conditions for MCS initiation

To investigate the circulation patterns favorable for MCS initiation, the daily circulations at 0000 UTC in JJA of 2018–2021 are objectively classified into 3 patterns by adopting the *k-means* algorithm, and the environmental parameters under different circulation patterns are further analyzed.

4.1 Objective classification of circulation patterns

Circulations of 285 days without direct influences from tropical cyclones in JJA of 2018–2021 are classified into 3 patterns according to the evaluation based on the silhouette coefficient, with 128, 66 and 91 days in each pattern, respectively, and the composite fields of geopotential height at 700 hPa are shown in Fig. 9.

Pattern-I (P1) is the typical circulation of the Mei-yu front (Fig. 9a). With a shallow trough in northeast China and the Indo-China Peninsula, the middle reaches of the YRB are in a large-scale convergence zone formed by the northwesterly flow from the high latitudes and the southwesterly flow from the low latitudes, which is consistent with the shear line and the strong equivalent potential temperature gradient. In Pattern-II (P2), the middle reaches of the YRB are basically under the control of the northwesterly, to the east of which is a deep trough (Fig. 9b). Although the equivalent potential temperature field also shows a strong gradient in P2, the thermodynamic characteristics of circulations in P1 and P2 are different. In P1, a warm humid air flow is dominated by the strong southwesterly, with a warm tongue extending from southwest to northeast. In P2, the northwesterly is the dominant wind, steering a cold tongue extending from north to south. The equivalent potential temperature field in P1 (336–348 K) is higher than that in P2 (332–340 K), indicating that the air mass in P1 is

warmer or moister than that in P2. In Pattern-III (P3), the middle reaches of the YRB are under the control of the weak southerly to the east of the Western Pacific Subtropical High.

Note that although circulations in P1 are related to the Mei-yu front, not all the MCSs are initiated within the Mei-yu frontal zone. In fact, many MCSs in P1 are initiated in the strong southwesterly flow to the south of the Mei-yu front rather than around the Mei-yu frontal zone. The mechanism for MCS initiations under such synoptic patterns may be related to the cold dome ahead of the Mei-yu front generated by previous convection, which promotes initiation by lifting high equivalent potential temperature air in the southwesterly flow to its level of free convection (Luo & Chen, 2015).

Of the 280 MCSs in P1, 72 (177) are initiated around (to the south of) the Mei-yu front, and the other 31 are initiated under the circulation without the Mei-yu front. For the MCSs initiated around or to the south of the Mei-yu front, the ratio of QS type to OM type is roughly the same, that is, 100/77 versus 40/32. Interestingly, of the MCSs initiated without the Mei-yu front, only 3 are OM type and the other 28 are QS type, suggesting that the OM MCSs are closely related to the Mei-yu front, whether they are initiated around it or to the south of it.

The MCSs in P2 are mostly initiated at the rear of the upper-level troughs, where a synoptic-scale low-level convergence zone/or low-pressure formed by the northerly flow and the southerly flow, favorable for small convective cells merging into a larger MCS (Maurer et al., 2017). As for the role of large-scale circulation in establishing instability, the case-by-case examination shows that in some cases the vertical structures of the upper-level troughs are tilted forward. Under the pattern of P2, the equivalent potential temperature decreases with height, creating convective instability. However, more information along with some in-depth study are required to confirm this conclusion.

A total of 330 QS MCSs and 187 OM MCSs are initiated during JJA of 2018–2021. Fifty percent of QS MCSs and 59.9% of OM MCSs are initiated in P1, suggesting that P1 is favorable for both QS and OM MCS initiation. Thirteen percent (36.1%) of the QS MCSs and 25.7% (14.4%) of the OM MCSs are initiated in P2 (P3). The daily average initiation frequencies of QS MCSs in the three patterns are 1.31, 0.65 and 1.31,

and those of the OM MCSs are 0.88, 0.72 and 0.3, respectively. In general, the QS MCS initiation in P1 and P3 is the same and in P2 is the least, while the OM MCSs are initiated the most in P1, followed by P2 and the least in P3.

Table 1. The number of days for each pattern and the total and daily occurrence for QS MCSs and OM MCSs in each pattern.

	P1 (128 days)	P2 (66 days)	P3 (91 days)
QS MCS	165 / 1.31	43 / 0.65	119 / 1.31
OM MCS	112 / 0.88	48 / 0.72	27 / 0.3

The synoptic-scale circulations in the middle reaches of YRB would be rather different in association with the several abrupt seasonal transition events during June to August (Hirasawa et al., 1995; Kawamura & Murakami, 1998; Zhang et al., 2020), which also affect the characteristics of MCSs' initiation, as being described in subsection 3.2. To further illustrate the seasonal changes in the appearance frequency of three circulation patterns and two types of MCSs, a time series in ten-day periods are shown in Fig. 9d. The occurrence frequency of P1 favors June and July, and that of P2 favors late July and August. As for P3, no notable seasonal changes are found. The occurrence frequency of OM MCSs peaks in late June or early July, and that of QS MCSs peaks variously in different years. Note that an extreme Mei-yu season in 2020 (Liu & Ding, 2020), featuring earlier onset, later retreat and abundant accumulated rainfall, and the occurrence frequencies of both P1 and OM MCSs are high in 2020. For the abnormal Mei-yu year (with a shorter duration and less rainfall) of 2018 (Zhao, 2019), the occurrence frequencies of both P1 and OM MCSs are lowest, with only one P1-type circulation and very few OM MCSs occurred after early July in 2018. The results imply that there are some connections between the Mei-yu front and the occurrence of P1 and OM MCSs.

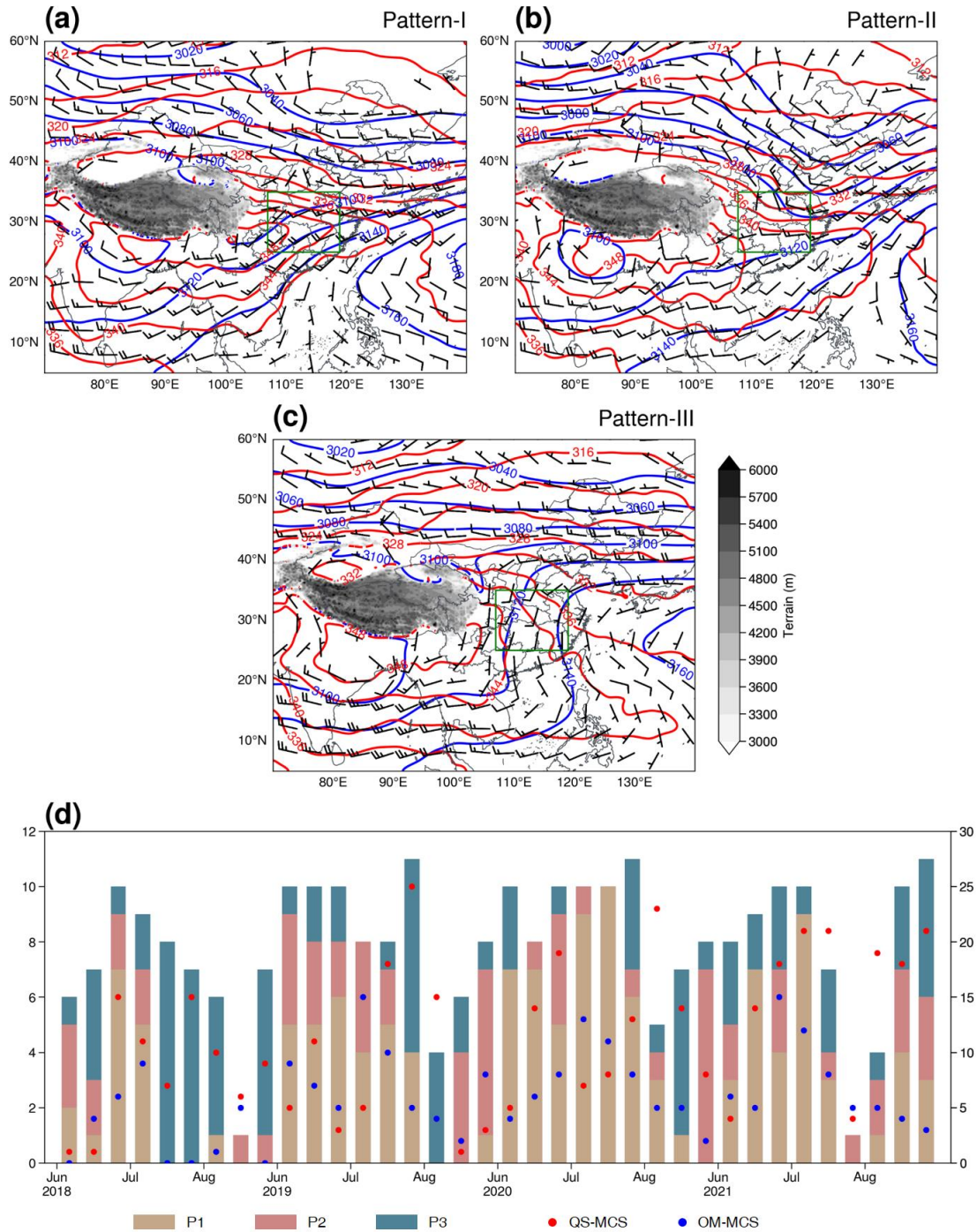


Figure 9. The composite geopotential fields (blue contours, gpm), equivalent potential temperature fields (red contours, K) and wind fields (wind barbs, m s⁻¹) at 700 hPa of P1 (a), P2 (b) and P3 (c), respectively. A half (full) barb represents 2 m s⁻¹ (4 m s⁻¹). The green rectangle marks the middle reaches of the YRB. The gray shading represents terrain heights (m). The bars (scatters) in (d) represent the occurrence frequency of three circulation patterns (two types of MCSs) over each ten-day period from June to August of 2018–2021, corresponding to the left (right) vertical axis. Note that for July and

August, the last ten-day period has 11 days.

4.2. Environmental parameters

To investigate the dynamic and thermodynamic conditions for MCS initiation under the three circulation patterns, ten environmental parameters are statistically analyzed, and the results are shown in Fig. 10.

The mean value of SBCAPE in P1 (Fig. 10 a) is 2363 J kg^{-1} and that of MUCAPE is 2491 J kg^{-1} , both the lowest in the three patterns. A low CAPE often implies a high LFC height or a small environmental lapse rate, yet the LFC height in P1 is the lowest in the three patterns (Fig. 10g) with a mean value of 743 m, which suggests that the lapse rate of the mid-low troposphere in P1 is small. The mean value of LI in P1 (Fig. 10e) is -4.4 K , the highest in the three patterns, which also confirms this conclusion. The mean PW in P1 (Fig. 10h) is 65 mm, which is significantly higher than those in P2 and P3. The contribution to the local water vapor growth in the YRB often came from the southwesterly and southeasterly originating from the oceans (Li et al., 2014; Shi et al., 2020; Wang et al., 2021), which is consistent with the synoptic circulation in P1.

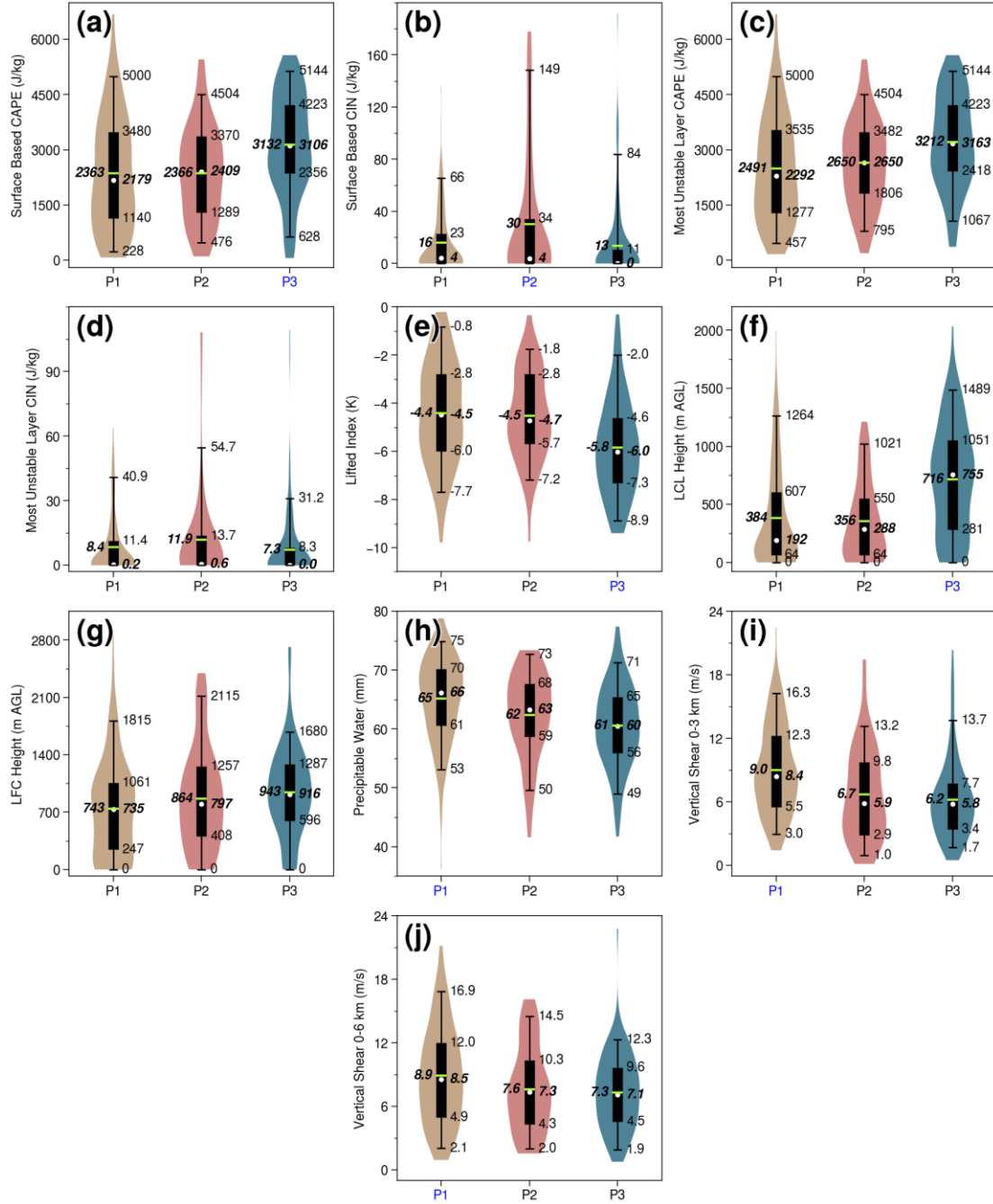
The mean SHR3 (Fig. 10i) and SHR6 (Fig. 10j) in P1 are 9 m s^{-1} and 8.9 m s^{-1} , respectively, which are both significantly higher than those in P2 and P3. In P2 and P3, the SHR6s are basically 1 m s^{-1} higher than the SHR3s (both the median and mean value). However, in P1, the medians of SHR6 and SHR3 are basically equal, and the mean values of SHR6 are even lower than those of SHR3. There is little difference between SHR3 and SHR6 in P1, but the SHR6s in P2 and P3 are higher than the SHR3s, which suggests that the wind speed in the low troposphere in P1 is high or that MCS initiation in P1 may often be accompanied by low-level jets. Higher vertical wind shears in P1 may be the reason why OM MCSs tend to occur in P1 (Cohen et al., 2007).

The mean SBCAPE (MUCAPE) in P2 is 2366 J kg^{-1} (2650 J kg^{-1}). The difference between MUCAPE and SBCAPE in P2 is the largest among the three patterns, indicating that the atmosphere in the boundary layer in P2 is more stable than those in P1 and P3, which is consistent with the composite circulation in P2, dominated by northerlies. In operational forecasts, a stable boundary layer and a low CAPE can be misleading and cause the possible elevated convections to be ignored. The mean SBCIN

in P2 is 30 J kg^{-1} (Fig. 10b), and the mean MUCIN in P2 is 11.9 J kg^{-1} (Fig. 10d), and both SBCIN and MUCIN were significantly higher than those in P1 and P3. In P2, 25% of MCSs are initiated in the environment with SBCIN greater than 34 J kg^{-1} (Fig. 10b). The large SBCIN in P2 confirms the aforementioned conclusion that the low-level atmosphere in P2 is more stable than those in P1 and P3. The mean LCL height in P2 (Fig. 10f) is 356 m, which is the lowest among the three patterns, and the mean LFC height (Fig. 10g) is 864 m. The lowest LCL height in P2 indicates a high relative humidity at the surface, which may be caused by the cold invasion related to the northerly.

Both the mean SBCAPE (Fig. 10a) and the mean MUCAPE (Fig. 10c) in P3 are 3132 J kg^{-1} and are significantly higher than those in P1 and P2. More than 25% of MCSs are initiated in the environment with SBCAPE over 4000 J kg^{-1} . The mean PW in P3 (Fig. 10h) is 61 mm, the mean SHR3 (Fig. 10i) is 6.2 m s^{-1} , and the mean SHR6 (Fig. 10j) is 7.3 m s^{-1} . Although different environmental parameters are not simply compensated for each other (Kirkpatrick et al., 2007), considering the lack of synoptic forcing and the lowest PW (Fig. 10j) in P3, a higher CAPE may be required during MCS initiation (Kirkpatrick et al., 2009; McCaul & Weisman, 2001). Furthermore, it is suggested that in an environment with a large CAPE, a higher LFC height and a lower PW are beneficial for updrafts (Kirkpatrick et al., 2011), which is similar to the configuration in P3. The mean LCL height (Fig. 10f) is 716 m and is significantly higher than those in P1 and P2. The highest LCL height in P3 suggests a relatively dry boundary layer (Rasmussen & Blanchard, 1998), causing stronger evaporation and colder outflow from the downdrafts (Kuchera & Parker, 2006) and further resulting in severe wind on the surface ground (Evans & Doswell, 2001; Kaltenböck et al., 2009). The difference between the mean LFC height and the mean LCL height is smallest in P3. A high LCL height suggests a dry low-level environment, and a low LFC height represents a large lapse rate, which indicates that in the warm and moist air mass, the surface solar heating in the afternoon leads to the high surface temperature and large lapse rate in the boundary layer, favoring the initiation of MCSs. The mean SBCIN (Fig. 10b) is 13 J kg^{-1} , and the mean MUCIN (Fig. 10d) is 7.3 J kg^{-1} , and both are at the minimum in the 3 patterns. Note that the medians of the SBCIN and the MUCIN in P3 are both 0 J kg^{-1} , which suggests that more than half of the MCSs in P3 are initiated in the environment with no CIN. However, the mean LFC height in P3 is the highest,

743 combined with the minimum CIN, representing a dry-adiabatic or even superadiabatic
744 low-level atmosphere.



745

746 **Figure 10.** Violin plots of environmental parameters. From (a) to (j) are SBCAPE (J kg^{-1}), SBCIN (J kg^{-1}), MUCAPE (J kg^{-1}), MUCIN (J kg^{-1}), LI (K), LCL (m), LFC (m),
747 kg^{-1}), SBCIN (J kg^{-1}), MUCAPE (J kg^{-1}), MUCIN (J kg^{-1}), LI (K), LCL (m), LFC (m),
748 PW (mm), SHR3 (m s^{-1}), and SHR6 (m s^{-1}). The outline of the violin represents the probability density. The upper and lower edges (caps) of the box (whiskers) inside the
749 violin represent the 3rd and 1st quartiles (95th and 5th percentiles), respectively, which
750 are marked on the right side of the violin. The white dot (lemon dash) inside the box
751

represents the median (mean value), which is marked in bold italics on the right (left). The pattern label marked blue indicates that the mean value of the parameter in this pattern is significantly (above the 95% level based on a two-tailed Welch's *t*-test) different from those in the other two patterns.

5 Summary and conclusions

Based on the BT data from the Advanced Geosynchronous Radiation Imager onboard the FY-4A satellite during the warm seasons (April–September) of 2018–2021, the combination of areal overlapping and optical flow is adopted to identify and track the MCSs in the middle reaches of the YRB, which are categorized into the quasistationary (QS) type and the outward-moving (OM) type and are statistically analyzed. The daily circulations of JJA, during which MCSs occur most frequently, are objectively classified into three patterns using the *k-means* algorithm, and the environmental conditions of MCS initiation are further compared and analyzed. The main conclusions are described as follows:

(1) During the warm seasons of 2018–2021, 524 QS MCSs and 276 OM MCSs are identified in the middle reaches of the YRB. Among the four kinds of main moving paths (i.e., northeast kind, southeast kind, northwest kind and southwest kind) of QS MCSs, the occurrence frequency in the southeast kind is the highest. The QS MCSs are mostly initiated over mountainous areas and then propagate to the plains. The moving trajectories of OM MCSs are classified into three kinds of paths, namely, the northeast kind, the southeast kind and the southwest kind, among which the southeast kind has the largest amount of OM MCSs.

(2) The QS MCSs primarily occur in July and August and are mainly initiated in the afternoon (0600–0700 UTC). The OM MCSs mostly occur in June and July with two initiation peaks at noon (0300–0500 UTC) and late night (1800–1900 UTC), respectively, corresponding to the afternoon peak and morning peak of the typical precipitation associated with Mei-yu fronts. QS MCSs are mainly initiated in mountainous areas, while OM MCSs are mostly triggered in plain areas.

(3) The OM MCSs move faster than the QS MCSs and mostly propagate eastward. The durations and maximum extents of QS MCSs show no obvious differences among different months, while those of OM MCSs vary among different

months. The lowest brightness temperatures of QS MCSs mostly appear in the afternoon (0800–0900 UTC), but those of the OM MCSs exhibit no obvious diurnal variation. Compared to the OM MCSs, the QS MCSs show notable diurnal variation in intensity and develop more rapidly.

(4) Circulations at 0000 UTC of 285 MCS days, without direct influences from tropical cyclones, are classified into 3 patterns using the k-means algorithm. The composite circulation of P1 is consistent with the typical circulation of the Mei-yu front, and those of P2 and P3 are dominated by the northwesterly and the weak southerly, respectively. The mean initiation frequencies of the QS MCSs in P1 and P3 are the same and that in P2 is the lowest. The OM MCSs are initiated the most in P1, followed by P2, and they are initiated the least in P3.

(5) Analysis of the environmental conditions favorable for MCS initiation in the three circulation patterns suggests that a) the low-level wind speed in P1 is relatively high, and the MCS initiations in P1 may be accompanied by low-level jets, which is more favorable for OM MCS initiation and propagation; b) the circulation in P2 is dominated by northwesterlies with a relatively stable layer in the low-level troposphere; and c) surface solar heating in P3 establishes a dry-adiabatic or even a superadiabatic layer and further lowers the stability.

In the present work, a comprehensive analysis was conducted on the MCSs in the middle reaches of the YRB during the warm seasons of 2018–2021, focusing mainly on the statistical characteristics, circulation patterns, and environmental conditions favorable for MCS initiation, and some conclusions with scientific significance and utility value were obtained. However, some problems remain unsolved. For example, the late-night triggering peak of OM MCSs is not well understood, and the impacts of orography on MCSs in the middle reaches of the YRB need further exploration. Further work will focus on these issues.

Acknowledgments

This research was supported by the National Natural Science Foundation of China (Grant U2142202, 41975056 and 41975057), and Youth Innovation Promotion Association, Chinese Academy of Sciences.

Data/Software Availability Statement

Data: The FY-4A BT data is obtained from <http://satellite.nsmc.org.cn/PortalSite/Data/Satellite.aspx> (Yang et al., 2017) with approval by the China Meteorological Administration. The TC best-track data is available at https://tcdata.typhoon.org.cn/zjljsjj_zlhq.html (Lu et al., 2021; Ying et al., 2014). Both of the above sites include translation functionality. The ERA5 hourly data on pressure levels is available at <https://doi.org/10.24381/cds.bd0915c6> (Hersbach et al., 2020). The ERA5 hourly data on single levels is available at <https://doi.org/10.24381/cds.adbb2d47> (Hersbach et al., 2020).

Software: Figures were made with ProPlot version 0.9.5 (Davis, 2021), licensed under CC-BY 4.0, available at <https://zenodo.org/record/5602155>. The optical flow was calculated by using OpenCV version 4.7.0 (Bradski, 2000) under the Apache License 2.0, available at <https://opencv.org>. The objective classification was made with scikit-learn version 1.2.2 (Pedregosa et al., 2011), available at <https://scikit-learn.org/stable/>. Environmental parameters were calculated by using MetPy version 1.5.0 (May et al., 2022) available at <https://doi.org/10.5065/D6WW7G29>.

References

- Akiyama, T. (1989). Large, Synoptic and Meso Scale Variations of the Baiu Front, during July 1982. *Journal of the Meteorological Society of Japan. Ser. II*, 67(1), 57–81. https://doi.org/10.2151/jmsj1965.67.1_57
- Asai, T., Ke, S., & Kodama, Y.-M. (1998). Diurnal Variability of Cloudiness over East Asia and the Western Pacific Ocean as Revealed by GMS during the Warm Season. *Journal of the Meteorological Society of Japan. Ser. II*, 76(5), 675–684. https://doi.org/10.2151/jmsj1965.76.5_675
- Astling, E. G. (1984). On the relationship between diurnal mesoscale circulations and precipitation in a mountain valley. *Journal of Applied Meteorology and Climatology*, 23(12), 1635–1644. [https://doi.org/10.1175/1520-0450\(1984\)023<1635:OTRBDM>2.0.CO;2](https://doi.org/10.1175/1520-0450(1984)023<1635:OTRBDM>2.0.CO;2)
- Augustine, J. A., & Howard, K. W. (1988). Mesoscale convective complexes over the United States during 1985. *Monthly Weather Review*, 116(3), 685–701.

- 843 [https://doi.org/10.1175/1520-0493\(1988\)116<0685:MCCOTU>2.0.CO;2](https://doi.org/10.1175/1520-0493(1988)116<0685:MCCOTU>2.0.CO;2)
- 844 Bai, L., Chen, G., & Huang, L. (2020). Convection initiation in monsoon coastal areas
845 (South China). *Geophysical Research Letters*, 47(11), e2020GL087035.
846 <https://doi.org/10.1029/2020GL087035>
- 847 Bao, X., Zhang, F., & Sun, J. (2011). Diurnal variations of warm-season precipitation
848 east of the Tibetan Plateau over China. *Monthly Weather Review*, 139(9), 2790–
849 2810. <https://doi.org/10.1175/MWR-D-11-00006.1>
- 850 Bechini, R., & Chandrasekar, V. (2017). An enhanced optical flow technique for radar
851 nowcasting of precipitation and winds. *Journal of Atmospheric and Oceanic*
852 *Technology*, 34(12), 2637–2658. <https://doi.org/10.1175/JTECH-D-17-0110.1>
- 853 Bernard, E., Naveau, P., Vrac, M., & Mestre, O. (2013). Clustering of maxima: spatial
854 dependencies among heavy rainfall in France. *Journal of Climate*, 26(20), 7929–
855 7937. <https://doi.org/10.1175/JCLI-D-12-00836.1>
- 856 Bister, M. (2001). Effect of peripheral convection on tropical cyclone formation.
857 *Journal of the Atmospheric Sciences*, 58(22), 3463–3476.
858 [https://doi.org/10.1175/1520-0469\(2001\)058<3463:EOPCOT>2.0.CO;2](https://doi.org/10.1175/1520-0469(2001)058<3463:EOPCOT>2.0.CO;2)
- 859 Bowler, N. E. H., Pierce, C. E., & Seed, A. (2004). Development of a precipitation
860 nowcasting algorithm based upon optical flow techniques. *Journal of Hydrology*,
861 288(1–2), 74–91. <https://doi.org/10.1016/j.jhydrol.2003.11.011>
- 862 Bradski, G. (2000). The OpenCV library [Software]. *Dr. Dobb's Journal of Software*
863 *Tools*. <https://www.drdobbs.com/open-source/the-opencv-library/184404319>
- 864 Brooks, H. E., Lee, J. W., & Craven, J. P. (2003). The spatial distribution of severe
865 thunderstorm and tornado environments from global reanalysis data. *Atmospheric*
866 *Research*, 67–68, 73–94. [https://doi.org/10.1016/S0169-8095\(03\)00045-0](https://doi.org/10.1016/S0169-8095(03)00045-0)
- 867 Brotzge, J. A., Nelson, S. E., Thompson, R. L., & Smith, B. T. (2013). Tornado
868 probability of detection and lead time as a function of convective mode and
869 environmental parameters. *Weather and Forecasting*, 28(5), 1261–1276.
870 <https://doi.org/10.1175/WAF-D-12-00119.1>

- 871 Burton, R. R., Blyth, A. M., Cui, Z., Groves, J., Lamptey, B. L., Fletcher, J. K.,
872 Marsham, J.H., Parker, D.J. & Roberts, A. (2022). Satellite-based nowcasting of
873 west African mesoscale storms has skill at up to 4-h lead time. *Weather and*
874 *Forecasting*, 37(4), 445–455. <https://doi.org/10.1175/WAF-D-21-0051.1>
- 875 Carbone, R. E., Tuttle, J. D., Ahijevych, D. A., & Trier, S. B. (2002). Inferences of
876 predictability associated with warm season precipitation episodes. *Journal of the*
877 *Atmospheric Sciences*, 59(13), 2033–2056. [https://doi.org/10.1175/1520-0469\(2002\)059<2033:IOPAWW>2.0.CO;2](https://doi.org/10.1175/1520-0469(2002)059<2033:IOPAWW>2.0.CO;2)
- 879 Cohen, A. E., Coniglio, M. C., Corfidi, S. F., & Corfidi, S. J. (2007). Discrimination of
880 mesoscale convective system environments using sounding observations. *Weather*
881 *and Forecasting*, 22(5), 1045–1062. <https://doi.org/10.1175/WAF1040.1>
- 882 Davis, L. L. B. (2021, October). ProPlot (Version 0.9.5). [Software]. *Zenodo*.
883 <https://doi.org/10.5281/zenodo.5602155>
- 884 Dong, Y., Li, J., Guo, J., Jiang, Z., Chu, Y., Chang, L., Yang, Y. & Liao, H. (2020). The
885 impact of synoptic patterns on summertime ozone pollution in the North China
886 Plain. *Science of The Total Environment*, 735, 139559.
887 <https://doi.org/10.1016/j.scitotenv.2020.139559>
- 888 Evans, J. S., & Doswell, C. A. (2001). Examination of derecho environments using
889 proximity soundings. *Weather and Forecasting*, 16(3), 329–342.
890 [https://doi.org/10.1175/1520-0434\(2001\)016<0329:EODEUP>2.0.CO;2](https://doi.org/10.1175/1520-0434(2001)016<0329:EODEUP>2.0.CO;2)
- 891 Feng, Z., Leung, L. R., Houze, R. A., Hagos, S., Hardin, J., Yang, Q., Han, B. & Fan, J.
892 (2018). Structure and evolution of mesoscale convective systems: sensitivity to
893 cloud microphysics in convection-permitting simulations over the United States.
894 *Journal of Advances in Modeling Earth Systems*, 10(7), 1470–1494.
895 <https://doi.org/10.1029/2018MS001305>
- 896 Feng, Z., Houze, R. A., Leung, L. R., Song, F., Hardin, J. C., Wang, J., Gustafson, W. I.
897 & Homeyer, C. R. (2019). Spatiotemporal characteristics and large-scale
898 environments of mesoscale convective systems east of the Rocky Mountains.
899 *Journal of Climate*, 32(21), 7303–7328. <https://doi.org/10.1175/JCLI-D-19-0137.1>

- 900 Fu, S., Sun, J., Zhao, S., & Li, W. (2011a). The energy budget of a southwest vortex
901 with heavy rainfall over south China. *Advances in Atmospheric Sciences*, 28(3),
902 709–724. <https://doi.org/10.1007/s00376-010-0026-z>
- 903 Fu, S., Sun, J., Zhao, S., Li, W. & Li, B. (2011b). A study of the impacts of the eastward
904 propagation of convective cloud systems over the Tibetan Plateau on the rainfall of
905 the Yangtze-Huai River basin. *Acta Meteorologica Sinica*, 69(4), 581–600,
906 <http://doi.org/10.11676/qxxb2011.051>. (in Chinese)
- 907 Gallus, W. A., Snook, N. A., & Johnson, E. V. (2008). Spring and summer severe
908 weather reports over the Midwest as a function of convective mode: a preliminary
909 study. *Weather and Forecasting*, 23(1), 101–113.
910 <https://doi.org/10.1175/2007WAF2006120.1>
- 911 Gensini, V. A., Mote, T. L., & Brooks, H. E. (2014). Severe-thunderstorm reanalysis
912 environments and collocated radiosonde observations. *Journal of Applied*
913 *Meteorology and Climatology*, 53(3), 742–751. [https://doi.org/10.1175/JAMC-D-](https://doi.org/10.1175/JAMC-D-13-0263.1)
914 [13-0263.1](https://doi.org/10.1175/JAMC-D-13-0263.1)
- 915 Grams, J. S., Thompson, R. L., Snively, D. V., Prentice, J. A., Hodges, G. M., & Reames,
916 L. J. (2012). A climatology and comparison of parameters for significant tornado
917 events in the United States. *Weather and Forecasting*, 27(1), 106–123.
918 <https://doi.org/10.1175/WAF-D-11-00008.1>
- 919 He, H., & Zhang, F. (2010). Diurnal variations of warm-season precipitation over
920 northern China. *Monthly Weather Review*, 138(4), 1017–1025.
921 <https://doi.org/10.1175/2010MWR3356.1>
- 922 He, Z., Zhang, Q., Bai, L., & Meng, Z. (2017). Characteristics of mesoscale convective
923 systems in central East China and their reliance on atmospheric circulation patterns.
924 *International Journal of Climatology*, 37(7), 3276–3290.
925 <https://doi.org/10.1002/joc.4917>
- 926 Hendricks, E. A., & Montgomery, M. T. (2006). Rapid scan views of convectively
927 generated mesovortices in sheared tropical cyclone Gustav (2002). *Weather and*
928 *Forecasting*, 21(6), 1041–1050. <https://doi.org/10.1175/WAF950.1>

- 929 Hersbach, H., Bell, B., Berrisford, P., Hirahara, S., Horányi, A., Muñoz-Sabater, J., et
930 al. (2020). The ERA5 global reanalysis [Dataset]. *Quarterly Journal of the Royal*
931 *Meteorological Society*, 146(730), 1999–2049. <https://doi.org/10.1002/qj.3803>
- 932 Hirasawa, N., Kato, K., & Takeda, T. (1995). Abrupt Change in the Characteristics of
933 the Cloud Zone in Subtropical East Asia around the Middle of May. *Journal of the*
934 *Meteorological Society of Japan. Ser. II*, 73(2), 221–239.
935 https://doi.org/10.2151/jmsj1965.73.2_221
- 936 Hoffmann, P., & Schlünzen, K. H. (2013). Weather pattern classification to represent
937 the urban heat island in present and future climate. *Journal of Applied Meteorology*
938 *and Climatology*, 52(12), 2699–2714. <https://doi.org/10.1175/JAMC-D-12-065.1>
- 939 Houze, R. A. (2004). Mesoscale convective systems. *Reviews of Geophysics*, 42(4).
940 <https://doi.org/10.1029/2004RG000150>
- 941 Huth, R., Beck, C., Philipp, A., Demuzere, M., Ustrnul, Z., Cahynová, M., et al. (2008).
942 Classifications of atmospheric circulation patterns. *Annals of the New York*
943 *Academy of Sciences*, 1146(1), 105–152. <https://doi.org/10.1196/annals.1446.019>
- 944 Jiang, J. & Fan, M. (2002). Convective clouds and mesoscale convective systems over
945 the Tibetan Plateau in summer. *Chinese Journal of Atmospheric Sciences*, 26(2),
946 263–270, <http://doi.org/10.3878/j.issn.1006-9895.2002.02.12>. (in Chinese)
- 947 Kaltenböck, R., Diendorfer, G., & Dotzek, N. (2009). Evaluation of thunderstorm
948 indices from ECMWF analyses, lightning data and severe storm reports.
949 *Atmospheric Research*, 93(1), 381–396. [https://doi.org/10.1016/](https://doi.org/10.1016/j.atmosres.2008.11.005)
950 [j.atmosres.2008.11.005](https://doi.org/10.1016/j.atmosres.2008.11.005)
- 951 Kanungo, T., Mount, D. M., Netanyahu, N. S., Piatko, C. D., Silverman, R., & Wu, A.
952 Y. (2002). An efficient k-means clustering algorithm: analysis and implementation.
953 *IEEE Transactions on Pattern Analysis and Machine Intelligence*, 24(7), 881–892.
954 <https://doi.org/10.1109/TPAMI.2002.1017616>
- 955 Kato, K., Matsumoto, J., & Iwasaki, H. (1995). Diurnal Variation of Cb-Clusters over
956 China and Its Relation to Large-Scale Conditions in the Summer of 1979. *Journal*
957 *of the Meteorological Society of Japan. Ser. II*, 73(6), 1219–1234.

- 958 https://doi.org/10.2151/jmsj1965.73.6_1219
- 959 Kawamura, R., & Murakami, T. (1998). Baiu near Japan and Its Relation to Summer
960 Monsoons over Southeast Asia and the Western North Pacific. *Journal of the*
961 *Meteorological Society of Japan. Ser. II*, 76(4), 619–639.
962 https://doi.org/10.2151/jmsj1965.76.4_619
- 963 King, A. T., & Kennedy, A. D. (2019). North American supercell environments in
964 atmospheric reanalyses and RUC-2. *Journal of Applied Meteorology and*
965 *Climatology*, 58(1), 71–92. <https://doi.org/10.1175/JAMC-D-18-0015.1>
- 966 Kirkpatrick, J. C., McCaul, E. W., & Cohen, C. (2007). The motion of simulated
967 convective storms as a function of basic environmental parameters. *Monthly*
968 *Weather Review*, 135(9), 3033–3051. <https://doi.org/10.1175/MWR3447.1>
- 969 Kirkpatrick, J. C., McCaul, E. W., & Cohen, C. (2009). Variability of updraft and
970 downdraft characteristics in a large parameter space study of convective storms.
971 *Monthly Weather Review*, 137(5), 1550–1561. [https://doi.org/10.1175/](https://doi.org/10.1175/2008MWR2703.1)
972 [2008MWR2703.1](https://doi.org/10.1175/2008MWR2703.1)
- 973 Kirkpatrick, J. C., McCaul, E. W., & Cohen, C. (2011). Sensitivities of simulated
974 convective storms to environmental CAPE. *Monthly Weather Review*, 139(11),
975 3514–3532. <https://doi.org/10.1175/2011MWR3631.1>
- 976 Kolios, S., & Feidas, H. (2010). A warm season climatology of mesoscale convective
977 systems in the Mediterranean basin using satellite data. *Theoretical and Applied*
978 *Climatology*, 102(1–2), 29–42. <https://doi.org/10.1007/s00704-009-0241-7>
- 979 Ku, H.-Y., Noh, N., Jeong, J.-H., Koo, J.-H., Choi, W., Kim, B.-M., et al. (2021).
980 Classification of large-scale circulation patterns and their spatio-temporal
981 variability during High-PM10 events over the Korean Peninsula. *Atmospheric*
982 *Environment*, 262, 118632. <https://doi.org/10.1016/j.atmosenv.2021.118632>
- 983 Kubota, H., & Nitta, T. (2001). Diurnal variations of tropical convection observed
984 during the TOGA-COARE. *Journal of the Meteorological Society of Japan. Ser. II*,
985 79(3), 815–830. <https://doi.org/10.2151/jmsj.79.815>

- 986 Kuchera, E. L., & Parker, M. D. (2006). Severe convective wind environments. *Weather*
987 *and Forecasting*, 21(4), 595–612. <https://doi.org/10.1175/WAF931.1>
- 988 Kukulies, J., Chen, D., & Curio, J. (2021). The role of mesoscale convective systems
989 in precipitation in the Tibetan Plateau region. *Journal of Geophysical Research:*
990 *Atmospheres*, 126(23), e2021JD035279. <https://doi.org/10.1029/2021JD035279>
- 991 Laing, A. G., & Michael Fritsch, J. (1997). The global population of mesoscale
992 convective complexes. *Quarterly Journal of the Royal Meteorological Society*,
993 123(538), 389–405. <https://doi.org/10.1002/qj.49712353807>
- 994 Lewis, M. W., & Gray, S. L. (2010). Categorisation of synoptic environments associated
995 with mesoscale convective systems over the UK. *Atmospheric Research*, 97(1–2),
996 194–213. <https://doi.org/10.1016/j.atmosres.2010.04.001>
- 997 Li, J., Yu, R., Zhou, T., & Wang, B. (2005). Why is there an early spring cooling shift
998 downstream of the Tibetan Plateau? *Journal of Climate*, 18(22), 4660–4668.
999 <https://doi.org/10.1175/JCLI3568.1>
- 1000 Li, X., Zhou, W., Chen, D., Li, C., & Song, J. (2014). Water vapor transport and
1001 moisture budget over eastern China: remote forcing from the two types of El Niño.
1002 *Journal of Climate*, 27(23), 8778–8792. [https://doi.org/10.1175/JCLI-D-14-](https://doi.org/10.1175/JCLI-D-14-00049.1)
1003 [00049.1](https://doi.org/10.1175/JCLI-D-14-00049.1)
- 1004 Li, Y., Wang, Y., Yang, S., Hu, L., Gao, S., & Fu, R. (2008). Characteristics of summer
1005 convective systems initiated over the Tibetan Plateau. Part I: origin, track,
1006 development, and precipitation. *Journal of Applied Meteorology and Climatology*,
1007 47(10), 2679–2695. <https://doi.org/10.1175/2008JAMC1695.1>
- 1008 Li, Z., Takeda, T., Tsuboki, K., Kato, K., Kawashima, M., & Fujiyoshi, Y. (2007).
1009 Nocturnal evolution of cloud clusters over eastern China during the intensive
1010 observation periods of GAME/HUBEX in 1998 and 1999. *Journal of the*
1011 *Meteorological Society of Japan. Ser. II*, 85(1), 25–45.
1012 <https://doi.org/10.2151/jmsj.85.25>
- 1013 Lin, X., Randall, D. A., & Fowler, L. D. (2000). Diurnal variability of the hydrologic
1014 cycle and radiative fluxes: comparisons between observations and a GCM. *Journal*

- 1015 of *Climate*, 13(23), 4159–4179. [https://doi.org/10.1175/1520-0442\(2000\)](https://doi.org/10.1175/1520-0442(2000)013<4159:DVOTHC>2.0.CO;2)
1016 [013<4159:DVOTHC>2.0.CO;2](https://doi.org/10.1175/1520-0442(2000)013<4159:DVOTHC>2.0.CO;2)
- 1017 Liu, N., Zhou, S., Liu, C., & Guo, J. (2019). Synoptic circulation pattern and boundary
1018 layer structure associated with PM_{2.5} during wintertime haze pollution episodes in
1019 Shanghai. *Atmospheric Research*, 228, 186–195.
1020 <https://doi.org/10.1016/j.atmosres.2019.06.001>
- 1021 Liu, Y., & Ding, Y. (2020). Characteristics and possible causes for the extreme Meiyu
1022 in 2020. *Meteorological Monthly*, 46(11), 1393–1404.
1023 <https://doi.org/10.7519/j.issn.1000-0526.2020.11.001> (in Chinese).
- 1024 Lu, X., Yu, H., Ying, M., Zhao, B., Zhang, S., Lin, L., et al. (2021). Western North
1025 Pacific tropical cyclone database created by the China Meteorological
1026 Administration [Dataset]. *Advances in Atmospheric Sciences*, 38(4), 690–699.
1027 <https://doi.org/10.1007/s00376-020-0211-7>
- 1028 Luo, Y., & Chen, Y. (2015). Investigation of the predictability and physical mechanisms
1029 of an extreme-rainfall-producing mesoscale convective system along the Meiyu
1030 front in East China: An ensemble approach. *Journal of Geophysical Research:*
1031 *Atmospheres*, 120(20), 10,593–10,618. <https://doi.org/10.1002/2015JD023584>
- 1032 Luo, Y., Wu, M., Ren, F., Li, J., & Wong, W.-K. (2016). Synoptic situations of extreme
1033 hourly precipitation over China. *Journal of Climate*, 29(24), 8703–8719.
1034 <https://doi.org/10.1175/JCLI-D-16-0057.1>
- 1035 Ma, R., Sun, J., & Yang, X. (2021a). A 7-yr climatology of the initiation, decay, and
1036 morphology of severe convective storms during the warm season over North China.
1037 *Monthly Weather Review*, 149(8), 2599–2612. [https://doi.org/10.1175/MWR-D-20-](https://doi.org/10.1175/MWR-D-20-0087.1)
1038 [0087.1](https://doi.org/10.1175/MWR-D-20-0087.1)
- 1039 Ma, R., Sun, J., & Yang, X. (2021b). An eight-year climatology of the warm-season
1040 severe thunderstorm environments over North China. *Atmospheric Research*, 254,
1041 105519. <https://doi.org/10.1016/j.atmosres.2021.105519>
- 1042 Machado, L. A. T., Rossow, W. B., Guedes, R. L., & Walker, A. W. (1998). Life cycle

- 1043 variations of mesoscale convective systems over the Americas. *Monthly Weather*
1044 *Review*, 126(6), 1630–1654. [https://doi.org/10.1175/1520-0493\(1998\)126<1630:](https://doi.org/10.1175/1520-0493(1998)126<1630:LCVOMC>2.0.CO;2)
1045 [LCVOMC>2.0.CO;2](https://doi.org/10.1175/1520-0493(1998)126<1630:LCVOMC>2.0.CO;2)
- 1046 Maddox, R. A. (1980). Mesoscale convective complexes. *Bulletin of the American*
1047 *Meteorological Society*, 61(11), 1374–1400. [https://doi.org/10.1175/1520-](https://doi.org/10.1175/1520-0477(1980)061<1374:MCC>2.0.CO;2)
1048 [0477\(1980\)061<1374:MCC>2.0.CO;2](https://doi.org/10.1175/1520-0477(1980)061<1374:MCC>2.0.CO;2)
- 1049 Mai Z., Fu, S., & Sun, J. (2020). Statistical features of two types of mesoscale
1050 convective systems (MCSs) generated over the eastern Tibetan Plateau during 16
1051 consecutive warm seasons. *Climatic and Environmental Research*, 25(4), 385–398,
1052 <http://doi.org/10.3878/j.issn.1006-9585.2019.19040>. (in Chinese)
- 1053 Marzban, C., & Sandgathe, S. (2010). Optical flow for verification. *Weather and*
1054 *Forecasting*, 25(5), 1479–1494. <https://doi.org/10.1175/2010WAF2222351.1>
- 1055 Maurer, V., Bischoff-Gauß, I., Kalthoff, N., Gantner, L., Roca, R., & Panitz, H.-J.
1056 (2017). Initiation of deep convection in the Sahel in a convection-permitting climate
1057 simulation for northern Africa: Deep Convection in the Sahel. *Quarterly Journal of*
1058 *the Royal Meteorological Society*, 143(703), 806–816.
1059 <https://doi.org/10.1002/qj.2966>
- 1060 May, R. M., Goebbert, K. H., Thielen, J. E., Leeman, J. R., Camron, M. D., Bruick, Z.,
1061 et al. (2022). MetPy: A meteorological python library for data analysis and
1062 visualization [Software]. *Bulletin of the American Meteorological Society*, 103(10),
1063 E2273–E2284. <https://doi.org/10.1175/BAMS-D-21-0125.1>
- 1064 McCaul, E. W., & Weisman, M. L. (2001). The sensitivity of simulated supercell
1065 structure and intensity to variations in the shapes of environmental buoyancy and
1066 shear profiles. *Monthly Weather Review*, 129(4), 664–687. [https://doi.org/10.1175/](https://doi.org/10.1175/1520-0493(2001)129<0664:TSOSSS>2.0.CO;2)
1067 [1520-0493\(2001\)129<0664:TSOSSS>2.0.CO;2](https://doi.org/10.1175/1520-0493(2001)129<0664:TSOSSS>2.0.CO;2)
- 1068 Mecikalski, J. R., & Bedka, K. M. (2006). Forecasting convective initiation by
1069 monitoring the evolution of moving cumulus in daytime GOES imagery. *Monthly*
1070 *Weather Review*, 134(1), 49–78. <https://doi.org/10.1175/MWR3062.1>
- 1071 Meng, Y., Sun, J., Zhang, Y., & Fu, S. (2021). A 10-year climatology of mesoscale

- convective systems and their synoptic circulations in the southwest mountain area of China. *Journal of Hydrometeorology*, 22(1), 23–41. <https://doi.org/10.1175/JHM-D-20-0167.1>
- Miao, Y., Guo, J., Liu, S., Liu, H., Li, Z., Zhang, W., & Zhai, P. (2017). Classification of summertime synoptic patterns in Beijing and their associations with boundary layer structure affecting aerosol pollution. *Atmospheric Chemistry and Physics*, 17(4), 3097–3110. <https://doi.org/10.5194/acp-17-3097-2017>
- Miller, D., & Fritsch, J. M. (1991). Mesoscale convective complexes in the western Pacific region. *Monthly Weather Review*, 119(12), 2978–2992. [https://doi.org/10.1175/1520-0493\(1991\)119<2978:MCCITW>2.0.CO;2](https://doi.org/10.1175/1520-0493(1991)119<2978:MCCITW>2.0.CO;2)
- Morake, D. M., Blamey, R. C., & Reason, C. J. C. (2021). Long-lived mesoscale convective systems over eastern South Africa. *Journal of Climate*, 1(aop), 1–66. <https://doi.org/10.1175/JCLI-D-20-0851.1>
- Morel, C., & Senesi, S. (2002). A climatology of mesoscale convective systems over Europe using satellite infrared imagery. I: Methodology. *Quarterly Journal of the Royal Meteorological Society*, 128(584), 1953–1971. <https://doi.org/10.1256/003590002320603485>
- Nga, P. T. T., Ha, P. T., & Hang, V. T. (2021). Satellite-based regionalization of solar irradiation in Vietnam by k-Means clustering. *Journal of Applied Meteorology and Climatology*, 60(3), 391–402. <https://doi.org/10.1175/JAMC-D-20-0070.1>
- Ning, G., Yim, S. H. L., Yang, Y., Gu, Y., & Dong, G. (2020). Modulations of synoptic and climatic changes on ozone pollution and its health risks in mountain-basin areas. *Atmospheric Environment*, 240, 117808. <https://doi.org/10.1016/j.atmosenv.2020.117808>
- Panosetti, D., Böing, S., Schlemmer, L., & Schmidli, J. (2016). Idealized large-eddy and convection-resolving simulations of moist convection over mountainous terrain. *Journal of the Atmospheric Sciences*, 73(10), 4021–4041. <https://doi.org/10.1175/JAS-D-15-0341.1>
- Pedregosa, F., Varoquaux, G., Gramfort, A., Michel, V., Thirion, B., Grisel, O., et al.

- 1101 (2011). Scikit-learn: Machine learning in python [Software]. *Journal of Machine*
 1102 *Learning Research*, 12, 2825–2830.
 1103 <https://dl.acm.org/doi/10.5555/1953048.2078195>
- 1104 Peters, J. M., & Schumacher, R. S. (2014). Objective categorization of heavy-rain-
 1105 producing MCS synoptic types by rotated principal component analysis. *Monthly*
 1106 *Weather Review*, 142(5), 1716–1737. <https://doi.org/10.1175/MWR-D-13-00295.1>
- 1107 Punkka, A.-J., & Bister, M. (2015). Mesoscale convective systems and their synoptic-
 1108 scale environment in Finland. *Weather and Forecasting*, 30(1), 182–196.
 1109 <https://doi.org/10.1175/WAF-D-13-00146.1>
- 1110 Rasmussen, E. N., & Blanchard, D. O. (1998). A baseline climatology of sounding-
 1111 derived supercell and tornado forecast parameters. *Weather and Forecasting*, 13(4),
 1112 1148–1164. [https://doi.org/10.1175/1520-0434\(1998\)013<1148:ABCOSD>](https://doi.org/10.1175/1520-0434(1998)013<1148:ABCOSD>2.0.CO;2)
 1113 [2.0.CO;2](https://doi.org/10.1175/1520-0434(1998)013<1148:ABCOSD>2.0.CO;2)
- 1114 Rehbein, A., Ambrizzi, T., & Mechoso, C. R. (2018). Mesoscale convective systems
 1115 over the Amazon basin. Part I: climatological aspects. *International Journal of*
 1116 *Climatology*, 38(1), 215–229. <https://doi.org/10.1002/joc.5171>
- 1117 Reif, D. W., & Bluestein, H. B. (2017). A 20-year climatology of nocturnal convection
 1118 initiation over the central and southern Great Plains during the warm season.
 1119 *Monthly Weather Review*, 145(5), 1615–1639. [https://doi.org/10.1175/MWR-D-16-](https://doi.org/10.1175/MWR-D-16-0340.1)
 1120 [0340.1](https://doi.org/10.1175/MWR-D-16-0340.1)
- 1121 Roberts, R. D., & Rutledge, S. (2003). Nowcasting storm initiation and growth using
 1122 GOES-8 and WSR-88D data. *Weather and Forecasting*, 18(4), 562–584.
 1123 [https://doi.org/10.1175/1520-0434\(2003\)018<0562:NSIAGU>2.0.CO;2](https://doi.org/10.1175/1520-0434(2003)018<0562:NSIAGU>2.0.CO;2)
- 1124 Rodgers, D. M., Howard, K. W., & Johnston, E. C. (1983). Mesoscale convective
 1125 complexes over the United States during 1982. *Monthly Weather Review*, 111(12),
 1126 2363–2369. [https://doi.org/10.1175/1520-0493\(1983\)111<2363:](https://doi.org/10.1175/1520-0493(1983)111<2363:MCCOTU>2.0.CO;2)
 1127 [MCCOTU>2.0.CO;2](https://doi.org/10.1175/1520-0493(1983)111<2363:MCCOTU>2.0.CO;2)
- 1128 Rodgers, E. B., Chang, S. W., Stout, J., Steranka, J., & Shi, J.-J. (1991). Satellite
 1129 observations of variations in tropical cyclone convection caused by upper-

- 1130 tropospheric troughs. *Journal of Applied Meteorology and Climatology*, 30(8),
 1131 1163–1184. [https://doi.org/10.1175/1520-0450\(1991\)030<1163:SOOVIT>](https://doi.org/10.1175/1520-0450(1991)030<1163:SOOVIT>2.0.CO;2)
 1132 [2.0.CO;2](https://doi.org/10.1175/1520-0450(1991)030<1163:SOOVIT>2.0.CO;2)
- 1133 Rousseeuw, P. J. (1987). Silhouettes: A graphical aid to the interpretation and validation
 1134 of cluster analysis. *Journal of Computational and Applied Mathematics*, 20, 53–65.
 1135 [https://doi.org/10.1016/0377-0427\(87\)90125-7](https://doi.org/10.1016/0377-0427(87)90125-7)
- 1136 Shen, Y., Du, Y., & Chen, G. (2020). Ensemble sensitivity analysis of heavy rainfall
 1137 associated with three MCSs coexisting over southern China. *Journal of*
 1138 *Geophysical Research: Atmospheres*, 125(2). [https://doi.org/10.1029/](https://doi.org/10.1029/2019JD031266)
 1139 [2019JD031266](https://doi.org/10.1029/2019JD031266)
- 1140 Shi, Y., Jiang, Z., Liu, Z., & Li, L. (2020). A Lagrangian analysis of water vapor sources
 1141 and pathways for precipitation in East China in different stages of the east Asian
 1142 summer monsoon. *Journal of Climate*, 33(3), 977–992. [https://doi.org/10.1175/](https://doi.org/10.1175/JCLI-D-19-0089.1)
 1143 [JCLI-D-19-0089.1](https://doi.org/10.1175/JCLI-D-19-0089.1)
- 1144 Sieglaff, J. M., Cronce, L. M., Feltz, W. F., Bedka, K. M., Pavolonis, M. J., & Heidinger,
 1145 A. K. (2011). Nowcasting convective storm initiation using satellite-based box-
 1146 averaged cloud-top cooling and cloud-type trends. *Journal of Applied Meteorology*
 1147 *and Climatology*, 50(1), 110–126. <https://doi.org/10.1175/2010JAMC2496.1>
- 1148 Solman, S. A., & Menéndez, C. G. (2003). Weather regimes in the South American
 1149 sector and neighbouring oceans during winter. *Climate Dynamics*, 21(1), 91–104.
 1150 <https://doi.org/10.1007/s00382-003-0320-x>
- 1151 Song, F., Feng, Z., Leung, L. R., Jr, R. A. H., Wang, J., Hardin, J., & Homeyer, C. R.
 1152 (2019). Contrasting spring and summer large-scale environments associated with
 1153 mesoscale convective systems over the U.S. Great Plains. *Journal of Climate*,
 1154 32(20), 6749–6767. <https://doi.org/10.1175/JCLI-D-18-0839.1>
- 1155 Stahl, K., Moore, R. D., & Mckendry, I. G. (2006). The role of synoptic-scale
 1156 circulation in the linkage between large-scale ocean–atmosphere indices and winter
 1157 surface climate in British Columbia, Canada. *International Journal of Climatology*,
 1158 26(4), 541–560. <https://doi.org/10.1002/joc.1268>

- 1159 Sugimoto, S., & Ueno, K. (2010). Formation of mesoscale convective systems over the
1160 eastern Tibetan Plateau affected by plateau-scale heating contrasts. *Journal of*
1161 *Geophysical Research: Atmospheres*, 115. <https://doi.org/10.1029/2009JD013609>
- 1162 Sun, J., & Zhang, F. (2012). Impacts of mountain–plains solenoid on diurnal variations
1163 of rainfalls along the mei-yu front over the East China plains. *Monthly Weather*
1164 *Review*, 140(2), 379–397. <https://doi.org/10.1175/MWR-D-11-00041.1>
- 1165 Sun J., Wei J., Fu S., Zhang Y. & Wang H., 2018: The multi-scale physical model for
1166 persistent heavy rainfall events in the Yangtze-Huaihe River valley. *Chinese*
1167 *Journal of Atmospheric Sciences*, 42(4), 741–754,
1168 <http://doi.org/10.3878/j.issn.1006-9895.1803.17246>. (in Chinese)
- 1169 Takeda, T., & Iwasaki, H. (1987). Some Characteristics of Meso-scale Cloud Clusters
1170 Observed in East Asia between March and October 1980. *Journal of the*
1171 *Meteorological Society of Japan. Ser. II*, 65(3), 507–513.
1172 https://doi.org/10.2151/jmsj1965.65.3_507
- 1173 Tao, S. (1980). *Heavy Rainfalls in China*. Beijing: Science Press.
- 1174 Ternynck, C., Alaya, M. A. B., Chebana, F., Dabo-Niang, S., & Ouarda, T. B. M. J.
1175 (2016). Streamflow hydrograph classification using functional data analysis.
1176 *Journal of Hydrometeorology*, 17(1), 327–344. [https://doi.org/10.1175/JHM-D-14-](https://doi.org/10.1175/JHM-D-14-0200.1)
1177 [0200.1](https://doi.org/10.1175/JHM-D-14-0200.1)
- 1178 Vandal, T., & Nemani, R. (2020). Temporal interpolation of geostationary satellite
1179 imagery with task specific optical flow. *Proceedings of 1st ACM SIGKDD*
1180 *Workshop on Deep Learning for Spatiotemporal Data, Applications, and Systems*
1181 *(DeepSpatial '20)*, 9 pp. [http://mason.gmu.edu/~lzhao9/venues/DeepSpatial2020/](http://mason.gmu.edu/~lzhao9/venues/DeepSpatial2020/papers/DeepSpatial_paper_6_camera_ready.pdf)
1182 [papers/DeepSpatial_paper_6_camera_ready.pdf](http://mason.gmu.edu/~lzhao9/venues/DeepSpatial2020/papers/DeepSpatial_paper_6_camera_ready.pdf)
- 1183 Velasco, I., & Fritsch, J. M. (1987). Mesoscale convective complexes in the Americas.
1184 *Journal of Geophysical Research: Atmospheres*, 92(D8), 9591–9613.
1185 <https://doi.org/10.1029/JD092iD08p09591>
- 1186 Wang, H., Sun, J., Fu, S., & Zhang, Y. (2021). Typical circulation patterns and
1187 associated mechanisms for persistent heavy rainfall events over Yangtze-Huaihe

- 1188 River Valley during 1981–2020. *Advances in Atmospheric Sciences*, 38(12), 2167–
1189 2182. <https://doi.org/10.1007/s00376-021-1194-8>
- 1190 Williams, M., & Houze, R. A. (1987). Satellite-observed characteristics of winter
1191 monsoon cloud clusters. *Monthly Weather Review*, 115(2), 505–519.
1192 [https://doi.org/10.1175/1520-0493\(1987\)115<0505:SOCOWM>2.0.CO;2](https://doi.org/10.1175/1520-0493(1987)115<0505:SOCOWM>2.0.CO;2)
- 1193 Wilson, J. W., & Roberts, R. D. (2006). Summary of convective storm initiation and
1194 evolution during IHOP: observational and modeling perspective. *Monthly Weather*
1195 *Review*, 134(1), 23–47. <https://doi.org/10.1175/MWR3069.1>
- 1196 Yang, J., Zhang, Z., Wei, C., Lu, F., & Guo, Q. (2017). Introducing the new generation
1197 of Chinese geostationary weather satellites, Fengyun-4 [Dataset]. *Bulletin of the*
1198 *American Meteorological Society*, 98(8), 1637–1658.
1199 <https://doi.org/10.1175/BAMS-D-16-0065.1>
- 1200 Yang, J., Zhao, K., Chen, X., Huang, A., Zheng, Y., & Sun, K. (2020). Subseasonal and
1201 diurnal variability in lightning and storm activity over the Yangtze River Delta,
1202 China, during mei-yu season. *Journal of Climate*, 33(12), 5013–5033.
1203 <https://doi.org/10.1175/JCLI-D-19-0453.1>
- 1204 Yang, R., Zhang, Y., Sun, J., & Li, J. (2020). The comparison of statistical features and
1205 synoptic circulations between the eastward-propagating and quasi-stationary MCSs
1206 during the warm season around the second-step terrain along the middle reaches of
1207 the Yangtze River. *Science China Earth Sciences*, 63(8), 1209–1222.
1208 <https://doi.org/10.1007/s11430-018-9385-3>
- 1209 Yang, X., Fei, J., Huang, X., Cheng, X., Carvalho, L. M. V., & He, H. (2015).
1210 Characteristics of mesoscale convective systems over China and its vicinity using
1211 geostationary satellite FY2. *Journal of Climate*, 28(12), 4890–4907.
1212 <https://doi.org/10.1175/JCLI-D-14-00491.1>
- 1213 Yang, X., & Sun, J. (2018). Organizational modes of severe wind-producing convective
1214 systems over North China. *Advances in Atmospheric Sciences*, 35(5), 540–549.
1215 <https://doi.org/10.1007/s00376-017-7114-2>
- 1216 Yang, Y., Wang, R., Chen, F., Liu, C., Bi, X., & Huang, M. (2021). Synoptic weather

- 1217 patterns modulate the frequency, type and vertical structure of summer precipitation
 1218 over Eastern China: a perspective from GPM observations. *Atmospheric Research*,
 1219 249, 105342. <https://doi.org/10.1016/j.atmosres.2020.105342>
- 1220 Ying, M., Zhang, W., Yu, H., Lu, X., Feng, J., Fan, Y., et al. (2014). An overview of the
 1221 China Meteorological Administration tropical cyclone database [Dataset]. *Journal*
 1222 *of Atmospheric and Oceanic Technology*, 31(2), 287–301.
 1223 <https://doi.org/10.1175/JTECH-D-12-00119.1>
- 1224 Yu, R., Zhou, T., Xiong, A., Zhu, Y., & Li, J. (2007). Diurnal variations of summer
 1225 precipitation over contiguous China. *Geophysical Research Letters*, 34(1).
 1226 <https://doi.org/10.1029/2006GL028129>
- 1227 Zhang, A., Chen, Y., Zhou, S., Cui, C., Wan, R., & Fu, Y. (2020). Diurnal variation of
 1228 meiyu rainfall in the Yangtze Plain during atypical meiyu years. *Journal of*
 1229 *Geophysical Research: Atmospheres*, 125(1), e2019JD031742.
 1230 <https://doi.org/10.1029/2019JD031742>
- 1231 Zhang, X., Shen, W., Zhuge, X., Yang, S., Chen, Y., Wang, Y., Chen, T., & Zhang, S.
 1232 (2021). Statistical characteristics of mesoscale convective systems initiated over the
 1233 Tibetan Plateau in summer by Fengyun satellite and precipitation estimates. *Remote*
 1234 *Sensing*, 13(9). <https://doi.org/10.3390/rs13091652>
- 1235 Zhang, X., Wang, X. L., & Corte-Real, J. (1997). On the relationships between daily
 1236 circulation patterns and precipitation in Portugal. *Journal of Geophysical Research:*
 1237 *Atmospheres*, 102(D12), 13495–13507. <https://doi.org/10.1029/97JD01012>
- 1238 Zhang, Y., & Sun, J. (2017). Comparison of the diurnal variations of precipitation east
 1239 of the Tibetan Plateau among sub-periods of Meiyu season. *Meteorology and*
 1240 *Atmospheric Physics*, 129(5), 539–554. [https://doi.org/10.1007/s00703-016-0484-](https://doi.org/10.1007/s00703-016-0484-7)
 1241 [7](https://doi.org/10.1007/s00703-016-0484-7)
- 1242 Zhang, Y., Zhang, F., & Sun, J. (2014). Comparison of the diurnal variations of warm-
 1243 season precipitation for East Asia vs. North America downstream of the Tibetan
 1244 Plateau vs. the Rocky Mountains. *Atmospheric Chemistry and Physics*, 14(19),
 1245 10741–10759. <https://doi.org/10.5194/acp-14-10741-2014>

- 1246 Zhang, Y., Zhang, F., Davis, C. A., & Sun, J. (2018). Diurnal evolution and structure of
1247 long-lived mesoscale convective vortices along the mei-yu front over the East China
1248 plains. *Journal of the Atmospheric Sciences*, 75(3), 1005–1025.
1249 <https://doi.org/10.1175/JAS-D-17-0197.1>
- 1250 Zhao, X. (2019). Characteristics and Causes Analysis of Abnormal Meiyu in China in
1251 2018. *Meteorological and Environmental Sciences*, 42(3), 29 – 33.
1252 <https://doi.org/10.16765/j.cnki.1673-7148.2019.03.004> (in Chinese)
- 1253 Zheng, L., Sun, J., Zhang, X., & Liu, C. (2013). Organizational modes of mesoscale
1254 convective systems over Central East China. *Weather and Forecasting*, 28(5),
1255 1081–1098. <https://doi.org/10.1175/WAF-D-12-00088.1>
- 1256 Zheng, Y., Chen, J., & Zhu, P. (2008). Climatological distribution and diurnal variation
1257 of mesoscale convective systems over China and its vicinity during summer.
1258 *Chinese Science Bulletin*, 53(10), 1574–1586. [https://doi.org/10.1007/s11434-008-](https://doi.org/10.1007/s11434-008-0116-9)
1259 [0116-9](https://doi.org/10.1007/s11434-008-0116-9)
- 1260 Zhu, L., Liu, J., Zhu, A., Sheng, M., & Duan, Z. (2018). Spatial distribution of diurnal
1261 rainfall variation in summer over China. *Journal of Hydrometeorology*, 19(4), 667–
1262 678. <https://doi.org/10.1175/JHM-D-17-0176.1>
- 1263 Zipser, E. J. (1977). Mesoscale and convective-scale downdrafts as distinct
1264 components of squall-line structure. *Monthly Weather Review*, 105(12), 1568–1589.
1265 [https://doi.org/10.1175/1520-0493\(1977\)105<1568:MACDAD>2.0.CO;2](https://doi.org/10.1175/1520-0493(1977)105<1568:MACDAD>2.0.CO;2)